

Spectral and photometric variability of SS 433 observed with XRISM and simultaneous optical and near-infrared telescopes

Yusuke SAKAI^{1,*}, Shinya YAMADA^{1,*}, Yuta OKADA^{2,*}, Toshihiro TAKAGI^{3,*}, Tomoya USUKI^{3,*}, Megumi SHIDATSU³, Shogo B. KOBAYASHI⁴, Robert PETRE⁵, Yoshihiro UEDA², Hideki UCHIYAMA⁶, Miho TAN^{7,8}, Taro KOTANI⁹, Taichi IGARASHI^{8,1}, Mami MACHIDA^{8,7}, Haruka SAKEMI¹⁰, Nobuyuki KAWAI¹¹, Daiki MIURA^{12,13}, Hiroya YAMAGUCHI^{13,12,14}, Kanta FUJIWARA², Daichi HIRAMATSU^{15,16,17}, Keisuke ISOGAI^{18,19}, Chulsoo KANG²⁰, Mariko KIMURA²¹, Katsuhiko L. MURATA¹⁸, Takahiro NAGAYAMA²², Taichi NAKAMOTO²⁰, Kosuke NAMEKATA^{23,24,25,26}, Yuki NIIDA²⁰, Yuu NIINO²⁷, Masafumi NIWANO⁸, Kyuseok OH²⁸, Shigeyuki SAKO^{29,30,31}, Mahito SASADA³², Hiromasa SUZUKI³³, Kenta TAGUCHI^{18,2}, Ichiro TAKAHASHI³⁴, Miyu UENISHI³, Yoichi YATSU³⁴, Marina YOSHIMOTO³

¹Department of Physics, Rikkyo University, 3-34-1 Nishi Ikebukuro, Toshima-ku, Tokyo 171-8501, Japan

²Department of Astronomy, Kyoto University, Kitashirakawa-Oiwake-cho, Sakyo-ku, Kyoto 606-8502, Japan

³Department of Physics, Ehime University, 2-5 Bunkyo-cho, Matsuyama, Ehime 790-8577, Japan

⁴Faculty of Physics, Tokyo University of Science, 1-3 Kagurazaka, Shinjuku-ku, Tokyo 162-8601, Japan

⁵NASA/Goddard Space Flight Center, Greenbelt, MD 20771, USA

⁶Faculty of Education, Shizuoka University, 836 Ohya, Suruga-ku, Shizuoka, Shizuoka 422-8529, Japan

⁷Astronomical Science Program, The Graduate University for Advanced Studies, SOKENDAI, 2-21-1 Osawa, Mitaka, Tokyo 181-8588, Japan

⁸Division of Science, National Astronomical Observatory of Japan, 2-21-1 Osawa, Mitaka, Tokyo 181-8588, Japan

⁹Kanagawa University, Faculty of Engineering, 3-27-1 Rokkakubashi, Kanagawa-ku, Yokohama, Kanagawa 221-8686, Japan

¹⁰Graduate School of Sciences and Technology for Innovation, Yamaguchi University, 1677-1 Yoshida, Yamaguchi 753-0841, Japan

¹¹Department of Physics, School of Science, Tokyo Institute of Technology, 2-12-1 Ookayama, Meguro-ku, Tokyo 152-8550, Japan

¹²Department of Physics, Graduate School of Science, The University of Tokyo, 7-3-1 Hongo, Bunkyo-ku, Tokyo 113-0033, Japan

¹³Institute of Space and Astronautical Science (ISAS), Japan Aerospace Exploration Agency (JAXA), 3-1-1 Yoshinodai, Chuo-ku, Sagami-hara, Kanagawa 252-5210, Japan

¹⁴Department of Science and Engineering, Graduate School of Science and Engineering, Aoyama Gakuin University, 5-10-1 Fuchinobe, Sagami-hara 252-5258, Japan

¹⁵Center for Astrophysics | Harvard & Smithsonian, 60 Garden Street, Cambridge, MA 02138-1516, USA

¹⁶The NSF AI Institute for Artificial Intelligence and Fundamental Interactions, USA

¹⁷Department of Astronomy, University of Florida, 211 Bryant Space Science Center, Gainesville, FL 32611-2055, USA

¹⁸Okayama Observatory, Kyoto University, 3037-5 Honjo, Kamogata-cho, Asakuchi, Okayama 719-0232, Japan

¹⁹Department of Multi-Disciplinary Sciences, Graduate School of Arts and Sciences, The University of Tokyo, 3-8-1 Komaba, Meguro, Tokyo 153-8902, Japan

²⁰Graduate School of Science and Engineering, Ehime University, 2-5, Bunkyo-cho, Matsuyama, Ehime 790-8577, Japan

²¹Advanced Research Center for Space Science and Technology, Institute of Science and Engineering, Kanazawa University, Kakuma, Kanazawa, Ishikawa 920-1192, Japan

²²Graduate School of Science and Engineering, Kagoshima University, 1-21-35 Korimoto, Kagoshima, Kagoshima 890-0065, Japan

²³Heliophysics Science Division, NASA Goddard Space Flight Center, 8800 Greenbelt Road, Greenbelt, MD 20771, USA

²⁴The Catholic University of America, 620 Michigan Avenue, N.E. Washington, DC 20064, USA

²⁵The Hakubi Center for Advanced Research, Kyoto University, Yoshida-Honmachi, Sakyo-ku, Kyoto 606-8501, Japan

²⁶Department of Physics, Kyoto University, Kitashirakawa-Oiwake-cho, Sakyo-ku, Kyoto 606-8502, Japan

²⁷Kiso Observatory, Institute of Astronomy, Graduate School of Science, The University of Tokyo, 10762-30 Mitake, Kiso, Nagano 397-0101, Japan

²⁸Korea Astronomy and Space Science Institute, Daedeokdae-ro 776, Yuseong-gu, Daejeon 34055, Republic of Korea

²⁹Institute of Astronomy, Graduate School of Science, The University of Tokyo, 2-21-1 Osawa, Mitaka, Tokyo 181-0015, Japan

³⁰UTokyo Organization for Planetary Space Science, The University of Tokyo, 7-3-1 Hongo, Bunkyo-ku, Tokyo 113-0033, Japan

³¹Collaborative Research Organization for Space Science and Technology, The University of Tokyo, 7-3-1 Hongo, Bunkyo-ku,

Tokyo 113-0033, Japan

³²Institute of Integrated Research, Institute of Science Tokyo, 2-12-1 Ookayama, Meguro-ku, Tokyo 152-8550, Japan

³³Faculty of Engineering, University of Miyazaki, Miyazaki 889-2192, Japan

³⁴Department of Physics, Institute of Science Tokyo, 2-12-1 Ookayama, Meguro-ku, Tokyo 152-8550, Japan

*E-mail: sakai.yusuke.d@rikkyo.ac.jp, syamada@rikkyo.ac.jp, okada.kusastro@gmail.com, takagi.toshihiro.bb@ehime-u.ac.jp, n809002b@mails.cc.ehime-u.ac.jp

ORCID: 0000-0002-5809-3516, 0000-0003-4808-893X, 0000-0001-8195-6546, 0000-0001-7773-9266, 0000-0003-3850-2041, 0000-0001-7821-6715, 0000-0003-4580-4021, 0009-0000-2006-2688, 0000-0003-4369-7314, 0000-0001-6353-7639, 0000-0002-4037-1346, 0009-0009-0439-1866, 0000-0002-5092-6085, 0009-0006-4377-4219, 0000-0002-1125-9187, 0000-0002-6480-3799, 0009-0002-1729-8416, 0000-0002-9579-731X, 0000-0002-1297-9485, 0000-0001-5322-5076, 0000-0003-3102-7452, 0000-0002-5037-951X, 0000-0002-8792-2205, 0000-0001-5946-9960, 0000-0002-8152-6172, 0000-0002-8482-8993, 0000-0003-2691-4444, 0000-0003-1890-3913, 0009-0005-0819-0819

Abstract

We present results from coordinated multiwavelength observations of the microquasar SS 433, obtained with XRISM, optical telescopes (Seimei, LCO, Tomo-e Gozen, MITSuME), and the kSIRIUS near-infrared camera during April 2024 and March 2025. The XRISM exposures amounted to ~ 200 ks in 2024 and ~ 100 ks in 2025, corresponding to different combinations of orbital and precessional phases. With XRISM/Resolve's high spectral resolution and large effective area, we clearly resolved numerous emission lines even in short time segments, achieving improved accuracy in Doppler-shift measurements relative to earlier observations. The simultaneously obtained X-ray and optical Doppler shifts suggest a possible tendency for the optical emission to lag slightly behind the X-rays. In the Resolve data, the Doppler shifts of the two jet components exhibited apparent asymmetries, with jet speeds fluctuating around $\sim 0.26 \pm 0.01c$ in 2024 and $\sim 0.30 \pm 0.01c$ in 2025. The velocity variations indicated modulations on a timescale of ~ 6.3 d, with a phase offset of about -90° relative to the nutation cycle. The observed line widths and flux of the approaching and receding jets appear consistent with the expected geometrical effects, indicating systematically larger line widths in the inner regions of the jets, as proposed by Shidatsu et al. (2025). Optical light curves show flares of ~ 400 s in 2024 and ~ 1600 s in 2025, with amplitudes up to $\sim 15\%$ during out-of-eclipse intervals, while the XRISM/Xtend light curves show no significant variability within the overlapping intervals and given the statistical uncertainties. Near-infrared photometry in 2024, obtained during an out-of-eclipse interval at a different epoch from the optical observations, showed no flare-like variability, and the X-ray band also remained constant within uncertainties. These coordinated observations provide a foundation for future XRISM studies aimed at probing the dynamical properties of the relativistic jets in SS 433.

Keywords: X-rays: binaries — stars: jets — stars: individual (SS 433) — accretion, accretion disks

1 Introduction

The microquasar SS 433 is one of the most intensively studied jet sources in our Galaxy, with over four decades of multi-wavelength observations (see reviews by Margon 1984; Fabrika 2004; Cherepashchuk et al. 2025). It is an X-ray binary consisting of an A-type supergiant and a compact object—either a black hole or a neutron star—in a 13.1-d orbit (Crampton & Hutchings 1981; Hillwig et al. 2004). A defining feature of the system is its baryonic jets, which show prominent Doppler-shifted emission lines in the X-ray, optical, and near-infrared bands. These jets precess with a period of 162.5 d, with an average bulk velocity of $\sim 0.26c$ (e.g., Abell & Margon 1979; Kotani et al. 1996; Marshall et al. 2002; Waisberg et al. 2019). The system is located at a distance of ~ 5.5 kpc (Blundell & Bowler 2004). On arcsecond scales ($\sim 10^{17}$ cm), the jets trace helical paths in radio and X-ray images (Hjellming & Johnston 1981; Sakai et al. 2025), while on degree scales (~ 100 pc) they inflate the surrounding W50 nebula through interactions with the interstellar medium (e.g., Geldzahler et al. 1980; Dubner et al. 1998; Brinkmann et al. 1996; Sakemi et al. 2023; Kayama et al. 2025).

In addition to precession and orbital motion, SS 433 also shows a 6.3-d nutation cycle, first proposed by Katz et al. (1982). These three periodicities together define the system's long-term kinematic behavior. Although generally stable, long-term optical (Cherepashchuk et al. 2022) and X-ray (Medvedev et al. 2019) monitoring has revealed subtle variations in jet properties, including phase shifts and small changes in the precession or nutation periods, on timescales of years. The physical origin of the nutation remains uncertain, with various models proposed to explain its nature and driving mechanisms (e.g., Collins & Newsom 1988; Eikenberry et al. 2001; Collins & Scher 2002).

The interpretation of nutation signatures depends on the spatial origin of the jet emission. In the optical band, emission is thought to arise from extended regions along the jet ($\sim 10^{14-15}$ cm; Fabrika

2004), leading to light-travel delays of up to ~ 0.5 d for the receding component. These delays complicate the isolation of intrinsic kinematic changes. X-ray emission lines, by contrast, are known to originate much closer to the launch point ($\sim 10^{12}$ cm; Brinkmann et al. 1991; Marshall et al. 2002), reducing geometric delays and providing a more direct view of the jet dynamics, although the emission may still be affected by obscuration from the companion star and/or accretion disk, whose dimensions can be comparable to those of the emission region (e.g., Fabrika 2004; Lopez et al. 2006).

Simultaneous optical and X-ray studies have provided important constraints on the spatial and dynamical structure of the jets. For example, Kubota et al. (2010) found a ~ 0.5 d delay between Suzaku X-ray and optical jet Doppler shifts, with short-term X-ray variations not fully explained by precession and nutation alone. Marshall et al. (2013) confirmed this delay and reported variations in the jet speed when compared with the symmetric jet model, which assumes that the two jets are ejected in opposite directions with the same velocity. Such deviations may arise from changes in jet speed, asymmetries between the jets, or motions of the launching region.

Photometric studies have also linked optical and X-ray variability in SS 433. Revnivtsev et al. (2004) and Atapin et al. (2015) detected rapid optical fluctuations with timescales similar to X-rays but delayed by ~ 100 s, which were interpreted as reprocessing of X-rays on the outer funnel walls into variable UV–optical emission. Burenin et al. (2011) found that the optical variability amplitude decreases during eclipses, implying a compact origin near the disk, and identified a break in the power spectral density at $f \approx 2.4 \times 10^{-3}$ Hz, corresponding to a timescale of ~ 70 s.

In this paper, we present a simultaneous multiwavelength campaign combining observations from the X-ray Imaging and Spectroscopy Mission (XRISM; Tashiro 2022) conducted in 2024 and 2025, alongside optical spectroscopy and minute-cadence

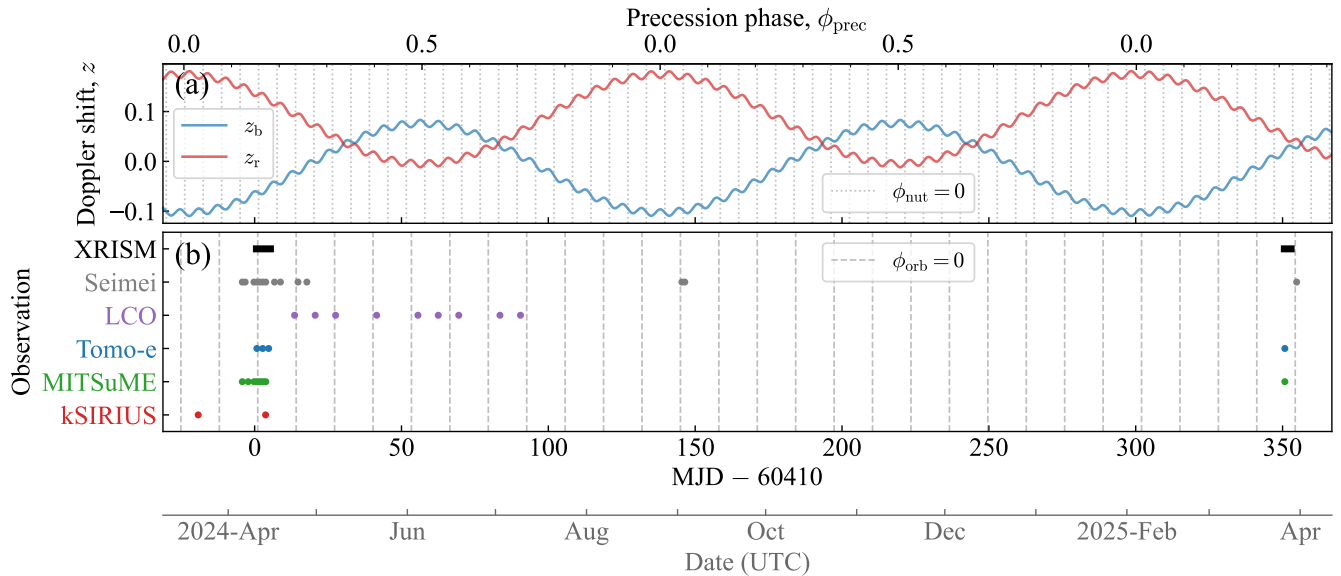


Fig. 1. Overview of the multiwavelength observation campaign of SS 433 conducted in 2024–2025. (a) Doppler shifts of the approaching and receding jets (z_b and z_r). The curves are calculated from the precession and nutation models based on the ephemerides and parameters of Gies et al. (2002) and Davydov et al. (2008), with the phase offset adjusted to match the observed Doppler shifts (see text). The dotted line indicates the nutation phase zero ($\phi_{\text{nut}} = 0$). (b) Timeline of observations. Observing epochs of XRISM (black), Seimei (gray), LCO (purple), Tomo-e Gozen (blue), MITSuME (green), and kSIRIUS (red) are shown. The dashed line indicates the orbital phase zero ($\phi_{\text{orb}} = 0$), based on the ephemeris of Cherepashchuk et al. (2023).

optical/near-infrared photometry. XRISM carries two instruments: the Resolve X-ray microcalorimeter (Ishisaki et al. 2022) and the Xtend X-ray CCD camera (Mori et al. 2022; Noda et al. 2025; Uchida et al. 2025), which we employed for high-resolution spectroscopy and X-ray light-curve measurements, respectively. XRISM/Resolve’s high spectral resolution and large effective area, as demonstrated in its first SS 433 analysis (Shidatsu et al. 2025), enable precise measurements of jet line widths in emission lines such as Si and Fe, allowing time-resolved spectroscopy with unprecedented sensitivity.

This paper is structured as follows. Section 2 describes the data reduction procedures. Section 3 presents time-resolved measurements of Doppler shifts in the jets, together with the analysis of light curves. Section 4 provides a discussion of our results. Finally, section 5 summarizes our conclusions. Unless otherwise noted, all quoted uncertainties correspond to 1σ confidence intervals.

2 Observations and data reduction

An overview of the X-ray, optical, and near-infrared observations of SS 433 is shown in figure 1. All times were standardized to Universal Time (UTC) for consistency across instruments.

2.1 XRISM

XRISM observations were carried out from 2024 April 10 to 15 (OBSID = 300041010) and from 2025 March 26 to 28 (OBSID = 201014010). The corresponding exposure times were ~ 204.3 ks and ~ 98.4 ks, respectively. Spectroscopic analysis was performed with the Resolve microcalorimeter, and light-curve data were obtained with the Xtend CCD camera. The data reduction was performed using HEASOFT version 6.34 and the XRISM Calibration Database available as of 2024 September, following the XRISM

Quick Start Guide v2.3¹.

We focused our spectral analysis on the Doppler-shifted Fe and Ni emission features from the jets using events in the 5.5–9 keV band. Although the Resolve bandpass extends down to ~ 1.6 keV even with the gate valve closed, time-resolved spectroscopy of lower-energy features such as Si and S lines would be challenging due to limited photon statistics. For the analysis, we used only the “High-resolution primary” (Hp) events, which are best calibrated in energy. The 6×6 pixel array includes one pixel dedicated to energy calibration. The response matrix file (RMF) was created using `rs1mkrmf` with the “large” configuration (`whichrmf=L`), and the ancillary response file (ARF) was generated using `xaarfgen`, assuming a point source at the aim point. Background subtraction was not applied, as the contributions from the non-X-ray background (NXB), cosmic X-ray background (CXB), and Galactic ridge X-ray emission (GRXE) were all estimated to be negligible. In particular, the NXB level was at most a few percent of the source flux in the 2–10 keV band, and the CXB and GRXE were even smaller.

We divided the Resolve data into time segments to investigate temporal variations in the emission lines. The number of segments was empirically chosen to balance temporal resolution and photon statistics: 30 for the brighter 2024 data and 5 for the fainter 2025 data. Each segment was assigned a sequential identification number (ID) starting from 0 (see table 3). The resulting exposure per segment was ~ 6.8 ks in 2024 and ~ 19.7 ks in 2025.

Xtend consists of four CCD chips arranged in a 2×2 configuration, providing a field of view of approximately 38.5×38.5 . It was operated in the full-window mode during both the 2024 and 2025 observations. Source events were extracted from a circular region with a $4'$ radius centered on SS 433, which was fully contained within a single CCD chip. We selected events in the 2–10 keV energy range to minimize contamination from the back-

¹ <https://heasarc.gsfc.nasa.gov/docs/xrism/analysis/quickstart/>

ground. Background subtraction was not applied, as the background contribution was estimated to be $\lesssim 5\%$ of the total count rate in this band.

2.2 Seimei

The Seimei telescope is a 3.8 m optical and near-infrared telescope located at Okayama Observatory, Kyoto University, Japan (Kurita et al. 2020). In this work, we conducted spectroscopy using the Kyoto Okayama Optical Low-dispersion Spectrograph with optical-fiber integral field unit (KOOLS-IFU; Yoshida 2005; Matsubayashi et al. 2019). The observations were conducted at 14 nights in total: 11 nights between 2024 April 5 and April 27, 2 nights on 2024 September 2 and 3, and 1 night on 2025 March 30. The VPH-blue grism, covering 4100–8900 Å with a wavelength resolution of $R \sim 500$ was adopted for all epochs, except for the observation on 2025 March 30, in which the VPH-683 grism, covering 5800–8000 Å with $R \sim 2000$ was utilized. The integration time for each object frame was 60 s, and we acquired between 3 (on 2024 April 27) and 50 (on 2024 April 12) frames per night.

We performed standard data reduction for all frames, including bias subtraction, flat-fielding, wavelength calibration, sky background subtraction, flux calibration, and barycentric correction, using IRAF (Tody 1986) and the KOOLS-IFU pipeline tool² to extract the spectra of the individual frames. The Hg, Ne and Xe comparison lamp data were used in the wavelength calibration. We adopted HR7596 as the standard star for the flux calibration, except for the nights of 2024 April 12 and 2025 March 30, for which HR5501 was adopted. In cases where bias, flat, comparison, or standard star frames were not available for a specific night, we utilized the corresponding data from the closest available night. We performed the above data reduction for the individual object frames, and adopted the spectra from a single object frame obtained at approximately the same time each night. The remaining spectra will be used in a separate paper to investigate intra-night variability.

2.3 LCO

Las Cumbres Observatory (LCO) operates a global network of robotic optical telescopes, comprising two 2 m, nine 1 m, and nine 0.4 m instruments distributed across six sites worldwide (Brown et al. 2013). In this work, we conducted spectroscopic observations using the FLOYDS, a cross-dispersed, low resolution spectrograph, mounted on the 2 m Faulkes Telescope North (FTN) at Haleakala (USA). The observations were conducted on 9 nights between April 23 and July 9, 2024. We used the spectra for the individual nights obtained through the FLOYDS pipeline³ (Valenti et al. 2014).

2.4 Tomo-e Gozen

Tomo-e Gozen is a wide-field CMOS mosaic camera mounted on the 1.05 m Kiso Schmidt telescope (Sako et al. 2018). It consists of 84 CMOS sensors, which cover approximately 30% of the focal plane and correspond to a circular field of view about 9° in diameter. Each sensor covers $39'.7 \times 22'.4$ with a pixel scale of $1''.19$, and all sensors are read simultaneously at 2 fps. The camera is sensitive to wavelengths from ~ 370 to 730 nm, peaking at 500 nm

(Kojima et al. 2018), and is particularly suited for detecting short-timescale transients through continuous sky monitoring.

Tomo-e Gozen observed SS 433 on April 10, 12, and 14, 2024, and on March 26, 2025. We obtained 23, 24, and 24 data cubes on the respective 2024 nights, and 69 cubes in 2025. Each cube nominally consists of 240 frames at 2 fps. Note that several data cubes from March 26 contain fewer than 240 frames due to elevated background levels during morning twilight. Standard pre-processing steps—including bias subtraction, dark correction, and flat-fielding—were applied. To balance photometric stability and temporal resolution, we stacked every 10 frames, corresponding to the typical PSF under average seeing conditions (FWHM $\sim 3\text{--}4''$). Aperture photometry was performed using a fixed 13-pixel radius ($\sim 15''$), centered on the targets.

Photometric zero-points were derived using Gaia DR3 G -band magnitudes (Gaia Collaboration et al. 2023). Although the Tomo-e Gozen response differs from the Gaia G -band, their spectral shapes are broadly similar, and this calibration method has been adopted in previous studies (e.g., Beniyama et al. 2022; Nishino et al. 2022). Since the same calibration stars were used across all frames, systematic offsets are expected to be uniform, ensuring reliable relative photometry. Stars with $G > 16.5$ were excluded to avoid sources near the detection limit. We also required no other cataloged object within $30''$ to minimize contamination and limited the calibration sample to stars with $9 < G < 14.5$. Instrumental fluxes were measured via aperture photometry, and the zero-point for each frame was computed by fitting the instrumental magnitudes to Gaia values. Frames with zero-point standard deviation exceeding 0.1 mag were discarded, and we retained only measurements with signal-to-noise ratio (S/N) > 10 to remove low-confidence outliers. A visual overview of the source environment around SS 433 is provided in appendix 1.

2.5 MITSuME

The Multicolor Imaging Telescopes for Survey and Monstrous Explosions (MITSuME) is a robotic optical telescope system consisting of 50-cm instruments (Kotani et al. 2005; Yatsu et al. 2007; Shimokawabe et al. 2009). Two telescopes are currently in operation, located at the Akeno Observatory and the Okayama Astrophysical Observatory, and are managed by the Institute of Science Tokyo and Kyoto University, respectively. Each telescope is equipped with three CCD cameras, enabling simultaneous photometric observations in the g' , R_C , and I_C bands. SS 433 was observed with MITSuME on April 5–13, 2024, and March 26, 2025. In 2024, both the Akeno and Okayama sites were used, while in 2025, observations were conducted only at Akeno. Exposure times of 10 s and 60 s per frame were adopted in 2024, whereas 10 s exposures were adopted in 2025. The 2025 dataset was obtained contemporaneously with XRISM and Tomo-e Gozen.

The data reduction for both telescopes was performed using a common automated analysis pipeline (Niwano et al. 2021). For the 10-second exposure data, every six consecutive frames (i.e., totaling 60 seconds of exposure time) were co-added to improve the S/N. The 60-second exposure data were analyzed on a frame-by-frame basis without co-adding. For consistency with the quality of the Tomo-e Gozen data, only the MITSuME data with S/N > 10 were used in the 2025 analysis. We also removed a single anomalous g' -band point near MJD 60760.80 that was significantly (~ 1 mag) brighter than the surrounding data, likely due to a photometric error. For the color index analysis presented in appendix 2, a more relaxed threshold of S/N > 3 was applied to the

² <https://www.kusastro.kyoto-u.ac.jp/~iwamuro/KOOLS/>

³ <https://lco.global/documentation/data/floyds-pipeline/>

2024 data. In addition, images co-added over an entire night were also prepared. Among these, the 2024 data were primarily used to trace the orbital phase and identify the timing of eclipses in the accretion disk. Aperture photometry was performed using relative photometry with reference to stars listed in the Pan-STARRS1 (PS1) catalog (Chambers et al. 2016) within the same field of view. For flux calibration, the catalog magnitudes in the PS1 g , r , and i bands were converted to the magnitudes in g' , R_C , and I_C bands following table 6 of Tonry et al. (2012). These magnitudes, initially in the AB system, were then converted to the Vega system using the offsets given in table 1 of Blanton & Roweis (2007).

2.6 kSIRIUS

kSIRIUS is a three-band (JHK_s) simultaneous imager mounted on the 1.0-m telescope at Kagoshima University (Nagayama & Nakaya 2024), providing a field of view of $\sim 3'.7 \times 2'.9$ with a pixel scale of $0''.69$ using dichroic beam splitters and InGaAs detectors. Monitoring observations were carried out on 2024 March 21 and April 13, employing a six-point dither pattern along the right ascension direction; the net exposure times were ~ 40 s and ~ 5600 s, respectively. Data reduction included dark subtraction, flat-fielding, sky subtraction from the dithered frames, and astrometric calibration using 2MASS (Cutri et al. 2003).

Photometric quality degraded after MJD 60413.755 (April 13), likely because of deteriorating sky conditions. To ensure reliability, all data taken after this time were excluded, removing approximately 30% of the frames and leaving a net usable exposure time of ~ 3900 s for that night. Aperture photometry was performed on the reduced images to extract light curves, yielding measurements with $S/N > 100$. All magnitudes are reported in the Vega system.

3 Analysis and results

3.1 Spectral analysis of X-ray and optical data

We measured the Doppler shifts of the approaching and receding jet components from time-resolved spectra in the X-ray and optical bands. Spectral fitting of the X-ray data obtained with Resolve was performed following the method described in Shidatsu et al. (2025), employing the optically thin, collisionally ionized plasma model APEC (Smith et al. 2001), supplemented by a stationary Fe I $K\alpha$ line. The model was fitted using XSPEC (Arnaud 1996) with the form $\text{tbabs}*(\text{bvapec_b} + \text{bvapec_r} + \text{gaussian})$, where bvapec_b and bvapec_r represent the eastern (approaching) and western (receding) jet components, respectively. The approaching and receding jets are hereafter referred to as the blue and red jets, respectively. The hydrogen column density was fixed at $2.07 \times 10^{22} \text{ cm}^{-2}$ (Lopez et al. 2006). The Fe I $K\alpha$ line was modeled with a Gaussian component, which was used as a simple approximation for a stationary narrow line possibly originating from the outer accretion disk (Kotani et al. 1996; Takagi et al. 2025). This line is known to have a FWHM $< 1000 \text{ km s}^{-1}$ (Marshall et al. 2002), and the Gaussian width was fixed to $\sigma_E = 10 \text{ eV}$ at 6.4 keV. We adopted the solar abundance table of Lodders et al. (2009) and the cross-section table of Verner et al. (1996). The Fe and Ni abundances in the plasma components were treated as free parameters. In particular, Ni has been reported to be overabundant relative to the solar value in SS 433 (e.g., Marshall et al. 2013; Shidatsu et al. 2025). The free parameters were the plasma temperature kT , Fe and Ni abundances (A_{Fe} , A_{Ni}), plasma normalizations N , Gaussian normalization N_{gau} , Doppler shift z , and

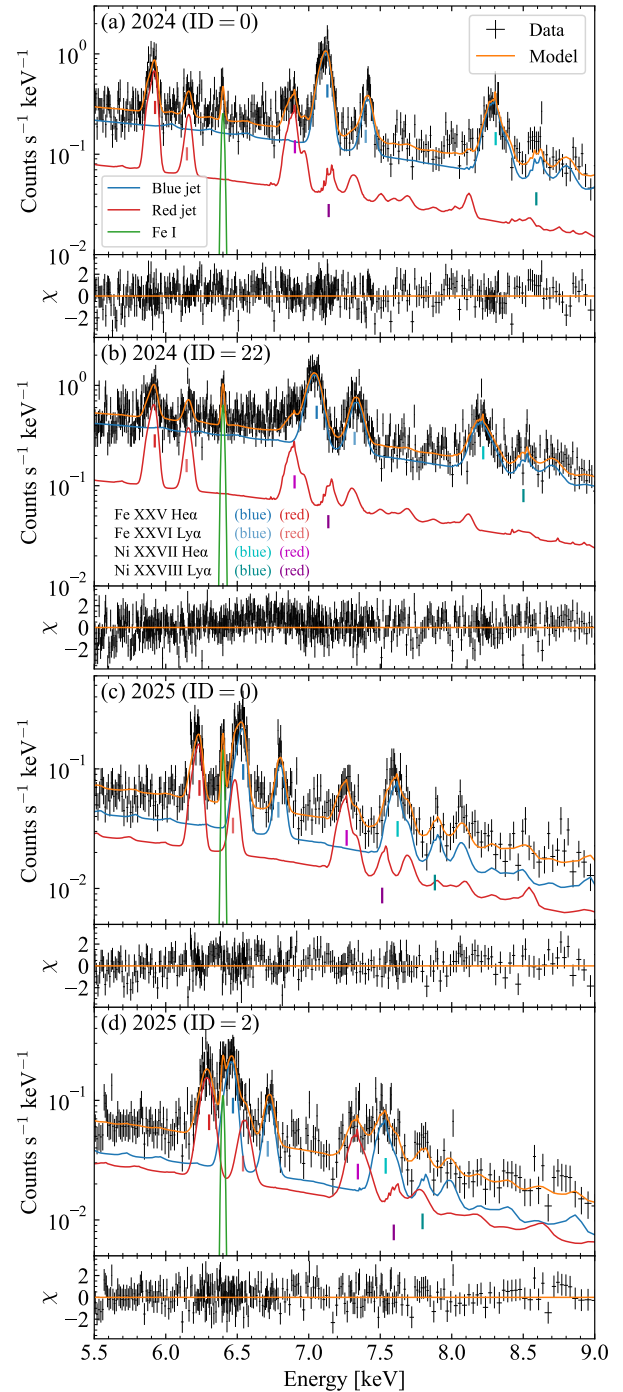


Fig. 2. XRISM/Resolve spectra from 2024 (a, b) and 2025 (c, d) represent time-resolved data, extracted from 30 intervals in 2024 and 5 in 2025. The panels show representative intervals: ID 0 and 22 (2024), and ID 0 and 2 (2025). The spectra are fitted with two thermal jet components and a stationary Fe line. Black points show the data; orange, the total model. Blue, red, and green lines represent the approaching jet, receding jet, and Fe I $K\alpha$, respectively. Several representative jet emission lines are overplotted based on the best-fit Doppler shifts. Representative Fe and Ni lines ($\text{He}\alpha$, $\text{Ly}\alpha$) are shown according to the best-fit Doppler model. Each panel shows the spectra with residuals.

the Gaussian sigma of the velocity broadening, σ_v . The corresponding FWHM is defined as $W_v = 2\sqrt{2\ln 2}\sigma_v$, and is used throughout this paper.

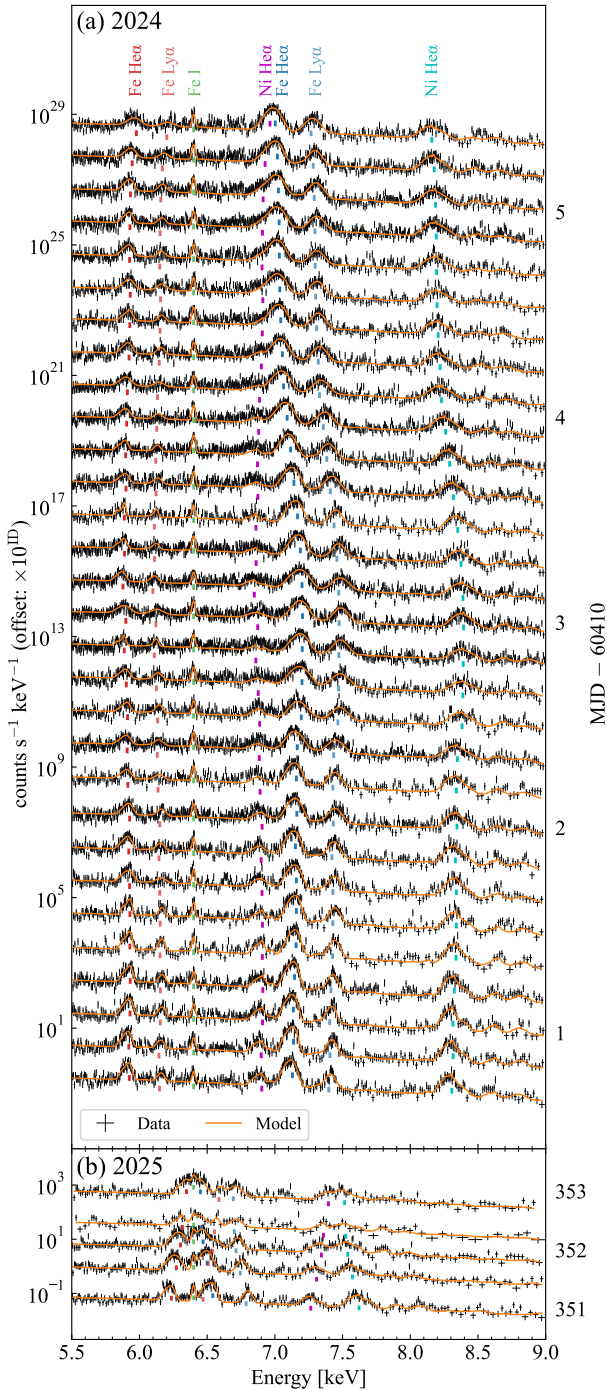


Fig. 3. Time-resolved XRISM/Resolve spectra in the 5.5–9 keV band from 2024 (a) and 2025 (b). The data are divided into 30 and 5 segments for the 2024 and 2025 observations, respectively, with vertical offsets applied to the black points for clarity. Spectra are fitted with two thermal jet components and a stationary Fe line (orange). Major emission lines are shown with the following colors: Fe XXV He α (blue/red), Fe XXVI Ly α (light blue/light red), and Ni XXVII He α (cyan/magenta), corresponding to the blue and red jets. The stationary Fe I K α line is shown in green. The right-hand axis shows the observation time in MJD. See table 3 for the Doppler shift values.

All parameters were linked between the two jet components, except for z , N , and W_{D} . More complex models, including multi-temperature plasma components or disk reflection, have been con-

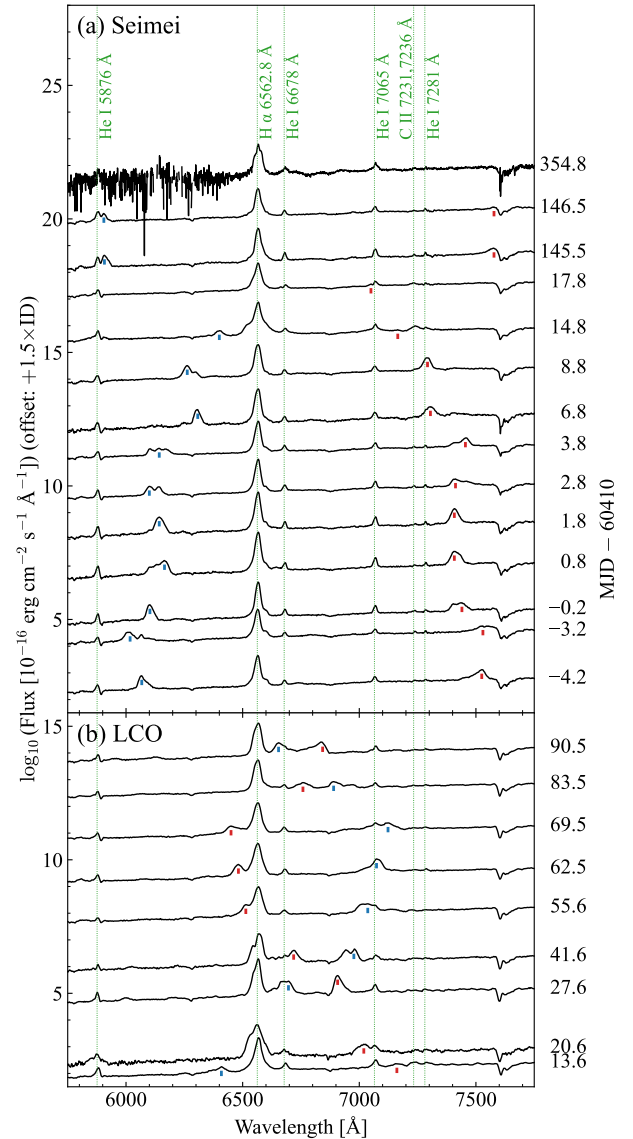


Fig. 4. Optical spectra obtained with the Seimei and LCO telescopes. The blue- and red-shifted components of the H α line are shown in blue and red, respectively. Dotted green lines indicate stationary emission lines such as He I, C II, and H α , which are likely associated with the accretion disk wind or circumbinary material. The right-hand axis shows the observation time in MJD for each spectrum. The corresponding Doppler shift values are summarized in table 4.

sidered in previous studies (e.g., Medvedev et al. 2018; Middleton et al. 2021). The model adopted in our analysis reproduces the spectral features sufficiently well for the purpose of Doppler shift measurements, although such more elaborate models will be explored in future work.

The fitting results are summarized in table 3. All parameters are generally consistent with those reported by (Shidatsu et al. 2025). The representative fitting results are presented in figures 2a and 2b for 2024 and figures 2c and 2d for 2025. The model components include the blue and red jets and the stationary Fe I K α line. In the 2024 observations, intervals ID 0 (during eclipse) and ID 22 (out of eclipse) clearly show the blue and red jet lines separately. Notably, the out-of-eclipse spectrum also exhibits a broader Fe XXV He α line, consistent with the findings of Shidatsu et al. (2025). In con-

trast, the 2025 spectra (IDs 0 and 2; out of eclipse) show only small Doppler shifts, indicating that the jets are oriented nearly perpendicular to the line of sight. During these epochs, the blue and red jet lines appear at similar energies due to the jets being nearly perpendicular to the observer's direction. The full set of fitting results is shown in figure 3. The corresponding full-band spectra for these epochs are shown in figure 17 (Appendix 3), which illustrates the overall spectral features.

For the optical spectra obtained with Seimei and LCO, the Doppler shifts of the blue and red jets were derived from the peak wavelengths of the corresponding H α line profiles, using the rest-frame wavelength of H α . Absorption features and nearby stationary components were visually inspected and accounted for when determining the peak positions. Three epochs were excluded from the analysis. In one case, both the blue and red jet components were excluded because the jet was nearly perpendicular to the line of sight, resulting in very weak emission with no clear peaks. In the other two cases, only the blue jet was excluded due to blending with stationary H α emission lines. The measured peak positions and corresponding Doppler shifts are shown in figure 4.

Table 1. Ephemeris and kinematic parameters adopted for SS 433

Parameter	Symbol	Value*
Precession[†]		
Period (d)	P_{prec}	162.15
Reference epoch (MJD) [†] (updated, this work) [#]	$t_{0,\text{prec}}$	51457.62 51467.67 \pm 0.01
Jet speed (c)	β	0.2602
Inclination angle ($^\circ$)	i	78.83
Half-opening angle ($^\circ$)	θ	19.85
Nutation[§]		
Period (d)	P_{nut}	6.287599
Reference epoch (MJD) [†] (updated, this work) [#]	$t_{0,\text{nut}}$	43029.655 43032.423 \pm 0.007
Amplitude (z)	A_{nut}	0.00689349
Orbit		
Period (d)	P_{orb}	13.08250
Period derivative (s s^{-1})	\dot{P}_{orb}	1.14×10^{-7}
Reference epoch (MJD) [†]	$t_{0,\text{orb}}$	51737.04

* Uncertainties reported in the original references are omitted here for clarity.

[†] Originally in JD, converted to MJD via $\text{MJD} = \text{JD} - 2400000.5$.

[‡] Ephemeris adopted from Gies et al. (2002).

[§] Ephemeris adopted from Davydov et al. (2008).

^{||} Ephemeris adopted from Cherepashchuk et al. (2023).

[#] Updated values derived from Doppler-shift analysis of XRISM/Resolve data (see subsection 3.2).

3.2 Doppler-shift variability in X-ray and optical

The temporal variability of the Doppler shifts is illustrated in figure 5. The blue jet shifts range from $z_b \sim -0.10$ to 0.08, and the red jet shifts from $z_r \sim -0.02$ to 0.15, exhibiting smooth periodic changes. In the 2024 X-ray and optical data, the Doppler-shift variations appear to have different amplitudes for the blue and red jets (likely related to variations in the jet velocity, which are examined in detail in subsection 4.4).

The Doppler shifts of SS 433 are often described by a commonly used kinematic model of jet precession (Abell & Margon

1979), with the nutation often represented phenomenologically by adding a sinusoidal term in redshift (e.g., Gies et al. 2002; Davydov et al. 2008). Such nutation is thought to arise from tidally driven torques from the companion star acting on the precessing disk (Katz et al. 1982). In practice, several modes may be present, but the ~ 6.3 -d component is dominant and is usually modeled by the sinusoidal term. This combined precession and nutation model can be expressed as

$$z = \gamma [1 \pm \beta (\cos i \cos \theta + \sin i \sin \theta \cos(2\pi\phi_{\text{prec}}))] - 1, \quad (1)$$

$$\delta z = \pm A_{\text{nut}} \sin(2\pi\phi_{\text{nut}}),$$

where $\beta = v/c$ is the intrinsic jet speed normalized to the speed of light, $\gamma = (1 - \beta^2)^{-1/2}$ is the Lorentz factor, i is the inclination angle of the jet axis with respect to the line of sight, and θ is the half-opening angle of the precession cone. The precession and nutation phases are defined as $\phi_{\text{prec}} = (t - t_{0,\text{prec}})/P_{\text{prec}}$ and $\phi_{\text{nut}} = (t - t_{0,\text{nut}})/P_{\text{nut}}$, with P_{prec} and P_{nut} denoting their respective periods. The total Doppler shift is given by $z + \delta z$, with the minus and plus signs corresponding to the blue and red jets, respectively.

To enable direct comparison with earlier determinations of the ephemerides, we applied this model to our data. In the fitting, β , i , θ , A_{nut} , P_{prec} , and P_{nut} were fixed to the tabulated values in table 1, as constrained by previous studies of the binary system, while $t_{0,\text{prec}}$ and $t_{0,\text{nut}}$ were treated as free parameters. The blue and red jets were fitted simultaneously under the assumption of shared model parameters, using all X-ray data from both the 2024 and 2025 observations. The resulting model curves are shown in figure 5. The updated reference epochs are summarized in table 1, showing offsets of about +10 d (precession; relative to Gies et al. 2002) and +2.8 d (nutation; relative to Davydov et al. 2008) with respect to the adopted ephemerides. Similar offsets have also been reported in previous studies (e.g., Kubota et al. 2010; Marshall et al. 2013; Cherepashchuk et al. 2018).

3.3 Simultaneous multiwavelength light curves

Simultaneous multiwavelength light curves were obtained during the campaign. The photometric results from all instruments are shown in figure 6. In the X-ray light curves (figure 6a), the 2024 data ($\phi_{\text{prec}} \sim 0.2$) show a higher count rate than the 2025 data ($\phi_{\text{prec}} \sim 0.3$), consistent with previous reports that the X-ray brightness varies with precession phase (e.g., Gies et al. 2002; Goranskij 2011).

In the optical bands (figures 6b and 6c), the light curves are primarily modulated by the orbital phase through eclipses, with additional variations in eclipse depth and overall brightness reported to depend on the precession phase (e.g., Cherepashchuk et al. 2025). Specifically, in the V band, during phases $|\phi_{\text{prec}}| < 0.2$, the brightness difference between eclipse and out-of-eclipse phases is typically $\Delta V \sim 0.6$ mag (e.g., Cherepashchuk et al. 2021), a trend also seen in the Tomo-e Gozen and MITSuME light curves. The photometric colors are consistent with previous studies (e.g., optical: Goranskij 2011; Cherepashchuk et al. 2025; near-infrared: Kodaira et al. 1985; Cherepashchuk et al. 2005). At similar orbital phases, the 2025 data are brighter by about ~ 0.1 mag compared to the 2024 data, without accompanying changes in the color indices.

To check the consistency of the orbital phase assignment (ϕ_{orb}), we adopted the ephemeris of Cherepashchuk et al. (2023), which includes the orbital period derivative (\dot{P}_{orb}). We compared the predicted eclipse timing with the 2024 MITSuME light curves and performed simple Gaussian fits near the eclipse phase ($|\phi_{\text{orb}}| <$

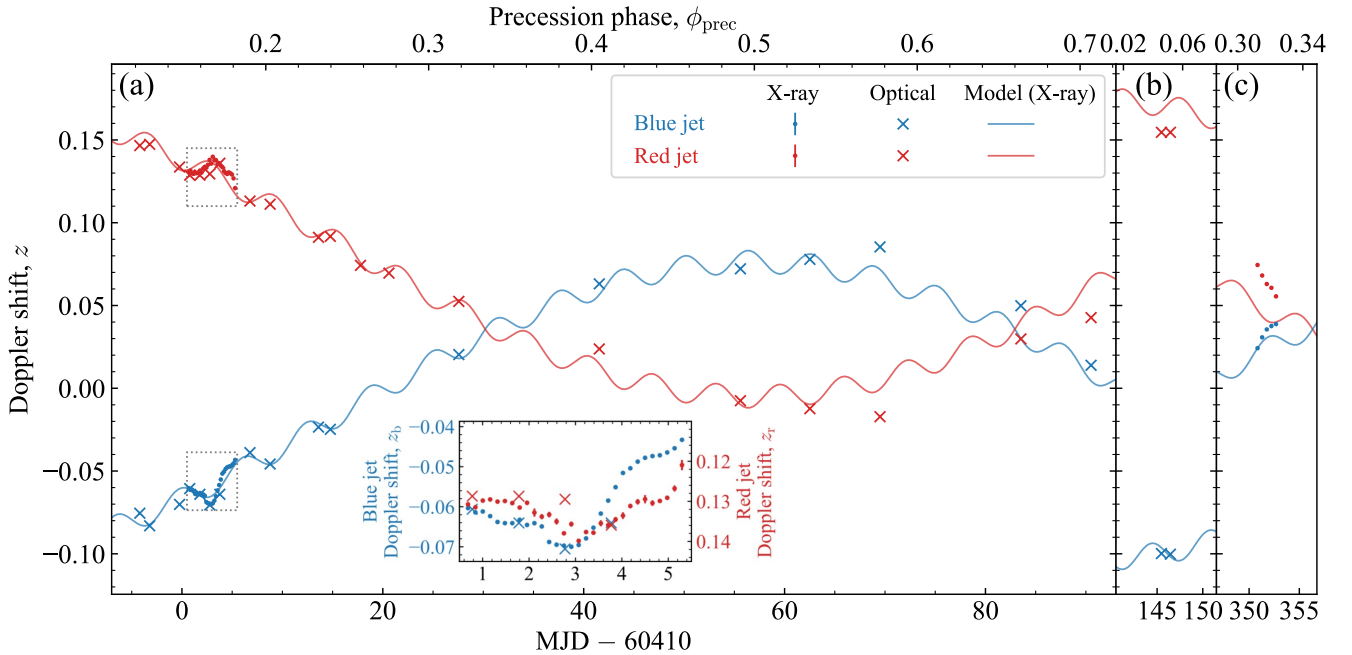


Fig. 5. Doppler shifts observed with XRISM/Resolve (X-ray) and Seimei/LCO (optical) from 2024 to 2025. (a–c) Blue and red data points indicate the blue and red jets, respectively. Panel (a) also includes an inset showing a zoom-in view of the blue and red jets within the highlighted rectangular region. The precession and nutation models are calculated based on the ephemeris and parameters from table 1, except for the reference epochs $t_{0,\text{prec}}$ and t_{nut} , which were fitted to the X-ray data as free parameters (see text).

0.15), following the procedure of Cherepashchuk et al. (2023). The fitted eclipse centers, shown in figure 6c, are $\phi_{\text{orb}} = 0.005 \pm 0.001$ in I_C , -0.001 ± 0.001 in R_C , and -0.01 ± 0.01 in g' , all consistent with $\phi_{\text{orb}} = 0$ within 1σ , except for the I_C band, which shows a slightly larger offset. However, given the limited number of data points near eclipse, this deviation is not considered significant. The 2024 X-ray light curve (figure 6a) also shows egress transitions consistent with this phase reference, supporting the validity of the Cherepashchuk et al. (2023) ephemeris for our dataset.

We now focus on the light curves obtained simultaneously with the X-ray data. Figure 7 presents the optical and X-ray light curves obtained in 2024. Panel (a) corresponds to the eclipse phase, while panels (b) and (c) show out-of-eclipse intervals. In panel (b), an optical flare with a timescale of ~ 400 s was observed, showing a flux enhancement of $\sim 15\%$ above the pre-flare level. Within the statistical uncertainties, no significant variability is seen in the X-ray light curve during the flare. The observed timescale and amplitude are similar to the R_C -band optical variability reported by Burenin et al. (2011). We also examined near-infrared light curves from kSIRIUS (figure 8) during the out-of-eclipse phase in 2024, finding that both the X-ray and near-infrared light curves showed no significant variability within the statistical uncertainties.

The optical and X-ray light curves obtained in 2025 are shown in figure 9. The Tomo-e Gozen light curve shows a clear brightening of $\sim 10\%$ over a timescale of ~ 1600 s. This brightening is also seen in the I_C and R_C bands from MITSuME, and the g' band shows no significant variation within the current signal-to-noise ratio. The X-ray coverage does not reach the optical peak, but the X-ray light curve stays flat during the overlap, similar to the optical trend. While the durations of the optical flares differ between 2024 and 2025, their rise and decay profiles are broadly similar. Given the limited number of detected events, interpretation of their physical origin is deferred to future investigations.

4 Discussion

4.1 Summary of observational results

We summarize the main results from our coordinated X-ray, optical, and near-infrared campaign on SS 433. Time-resolved spectroscopy was conducted with XRISM/Resolve in X-rays and simultaneously with Seimei and LCO in the optical. The X-ray spectra were divided into multiple time segments with typical exposures on the order of 10 ks, from which the jet Doppler shifts were obtained by fitting thermal plasma emission models. In the optical band, the shifts were measured from the peak positions of the $H\alpha$ emission lines. The statistical accuracy of the X-ray measurements reached $\Delta z \lesssim 3 \times 10^{-4}$ per segment, allowing variability on the nutation timescale to be probed. The X-ray and optical Doppler shifts showed closely aligned variations of both the blue and red jets. Applying the standard model of Doppler-shift variations, in which precession is supplemented by a sinusoidal nutation term (equation (1)), yielded phase offsets of a few days relative to the ephemerides of Gies et al. (2002) and Davydov et al. (2008), consistent with previous results.

Photometric observations with Tomo-e Gozen, MITSuME, and kSIRIUS indicated that the optical and near-infrared colors, as well as the eclipse timings, were broadly consistent with earlier studies. The optical data also revealed short-timescale flares with durations of ~ 400 – 1600 s and amplitudes up to $\sim 15\%$ in both 2024 and 2025. Although face-on configurations are generally associated with higher optical fluxes, the 2025 edge-on observations were brighter by ~ 0.1 mag compared to the 2024 data at similar orbital phases, without significant changes in color indices. This behavior cannot be readily explained by a geometrically thin disk model, in which the projected emitting area would be expected to decrease toward edge-on phases.

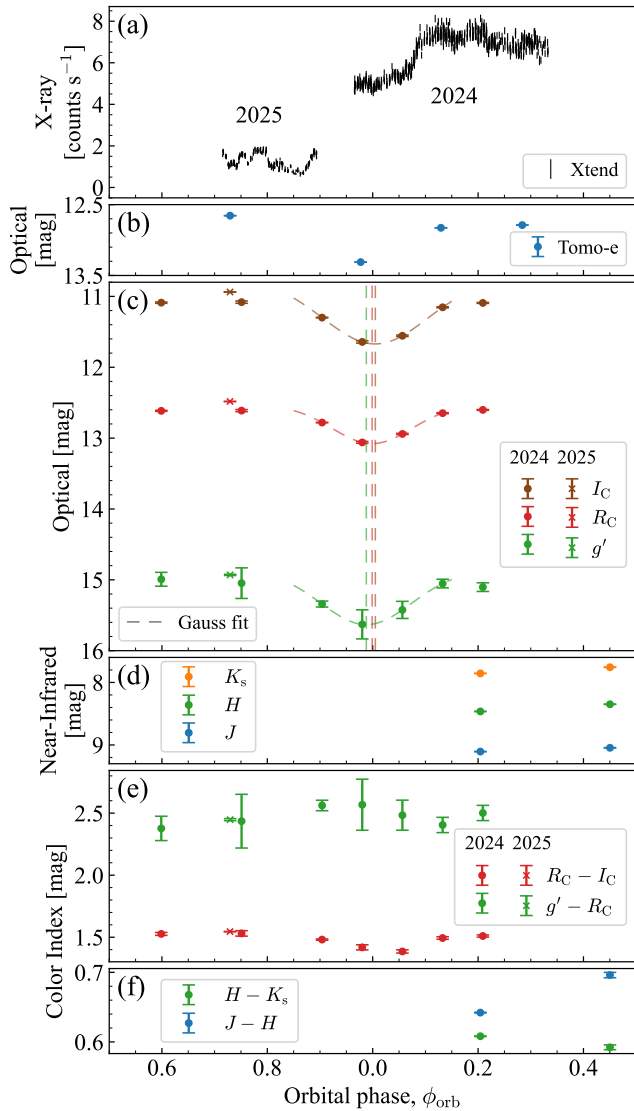


Fig. 6. Summary of simultaneous X-ray, optical and near-infrared observations conducted in 2024 and 2025. The orbital phase is calculated based on the ephemeris from Cherepashchuk et al. (2023). (a) XRISM/Xtend light curve in the 2–10 keV band. (b) Tomo-e Gozen optical light curve. (c) MITSuME optical light curves in the I_C (brown), R_C (red), and g' (green) bands. Dashed curves represent Gaussian fits to the MITSuME data obtained in April 2024 within $|\phi_{\text{orb}}| < 0.15$, and vertical dashed lines mark the fitted eclipse center times (see text). (d) kSIRIUS near-infrared light curves in the K_s (orange), H (green), and J (blue) bands. (e) Color indices derived from panel (c), calculated as $R_C - I_C$ (red) and $g' - R_C$ (green). (f) Color indices derived from panel (d), calculated as $H - K_s$ (green) and $J - H$ (blue).

4.2 X-ray vs. optical Doppler shifts and the impact of eclipse

A comparison between the temporal variations of Doppler shifts in the X-ray and optical bands provides important constraints on the spatial extent and physical conditions of the emitting regions. In previous studies, Kubota et al. (2010) analyzed Suzaku/XIS CCD spectra and, because of the limited energy resolution available at that time, modeled the data by superimposing Fe and Ni emission lines with Gaussian components on a continuum. They reported a delay of ~ 0.5 d in the optical Doppler shifts relative to the X-rays.

Furthermore, Chandra/HETG grating spectroscopy (Marshall et al. 2013) examined Mg XII, Si XIV, and Fe XXVI Ly α lines, as well as the Fe XXV He α line, and derived an upper limit of $\lesssim 0.4$ d for such a lag.

In the simultaneous XRISM/Resolve and optical observations in 2024, the superior spectral resolution and effective area of Resolve enabled direct application of physical plasma models to the time-resolved spectra. A magnified view of the Doppler-shift variations is shown in figures 10a and 10b, showing the same data and model as presented in figure 5. The high spectral resolution of Resolve allowed us to identify a large number of emission lines with high fidelity enabled a significant improvement in the accuracy of Doppler shift measurements compared with earlier studies. The results support the trend previously reported by Kubota et al. (2010) and Marshall et al. (2013), in which the optical Doppler shifts lag behind the X-rays. Future longer-duration monitoring covering different precessional phases will be required to establish the presence and possible phase dependence of such a delay with higher statistical significance.

The 2024 observation covered the egress, allowing us to test possible effects of partial occultation on the measured Doppler shifts. If different velocity layers along the jet were selectively blocked by the companion, a sharp change in the Doppler shift could appear across the eclipse, but no significant variation is seen. For a companion radius of order $\sim 10^{12-13}$ cm (e.g., Burenin et al. 2011), the expected light-travel delay is at most a few hundred seconds, which is an order of magnitude shorter than the time resolution of our spectral analysis. Therefore, the smooth evolution of the Doppler shift observed across the egress is consistent with the absence of detectable time-delay effects.

4.3 Geometrical interpretation of jet flux and line broadening

Following Shidatsu et al. (2025), who reported that the line widths of Fe and Ni lines (5.5–9 keV band) are larger than those of Si and S lines (2–4 keV band), and that the blue jet shows broader lines than the red jet in the 2024 data, we investigate how these line-broadening properties are related to the jet fluxes derived from the Resolve spectra (figure 3, table 3).

Figures 11a and 11b show the measured line widths of the blue (W_{v_b}) and red (W_{v_r}) jets. In 2024, the blue jet exhibited a slightly larger velocity width than the red jet, consistent with the tendency reported by Shidatsu et al. (2025), whereas in 2025 the velocity widths of the two jets were nearly identical. The corresponding 5.5–9 keV fluxes (F_b and F_r) are shown in figures 11c and 11d. In 2024, the blue jet showed a stronger flux contrast between the in-eclipse and out-of-eclipse phases than the red jet, whereas in 2025 both jets exhibited similar brightness and variability throughout the observation.

Since the observed jet fluxes are affected by Doppler beaming, we examined whether the measured flux variations can be explained by this effect. In this framework, each jet flux scales as $F \propto D^{n+\Gamma}$, where $D = 1/(1+z)$ is the Doppler factor calculated from the Doppler shifts of the blue and red jets measured in our spectral analysis. Here, n represents the jet emission state ($n = 2$ for a continuous flow and $n = 3$ for discrete blobs; e.g., Sikora et al. 1997). We considered both cases of $n = 2$ and $n = 3$. Although various interpretations of the appropriate value of n have been discussed in the literature (e.g., Miller-Jones et al. 2008), the difference is negligible for the present discussion, and we do not attempt to distinguish between them. Γ is the photon index, roughly 1.7 for

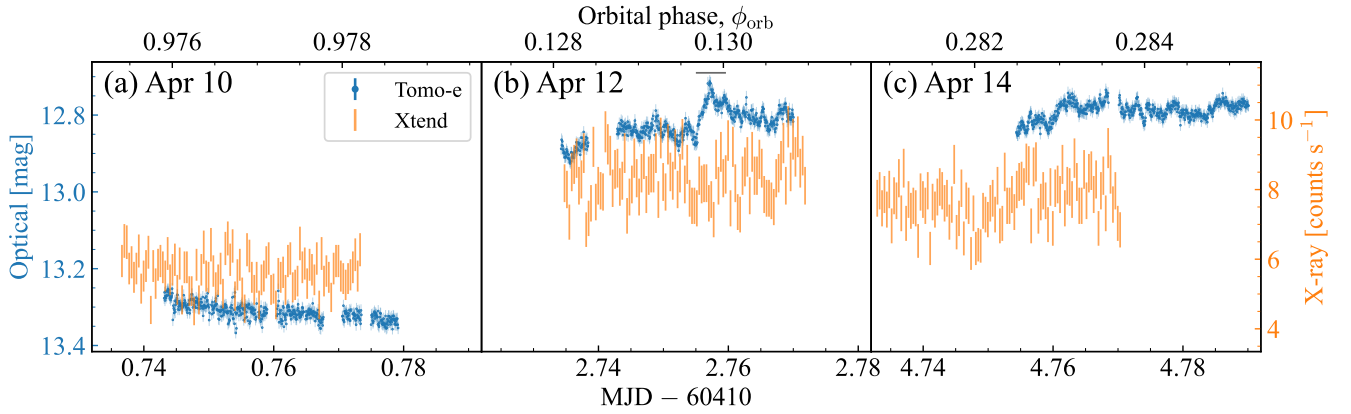


Fig. 7. Light curves obtained with Tomo-e Gozen and XRISM/Xtend in 2024. (a)–(c) correspond to April 10, 12, and 14, 2024, respectively, showing optical data from Tomo-e Gozen (blue) and X-ray data from XRISM/Xtend (orange; 2–10 keV, 32 s bins). In panel (b), an optical flare is visible, with a 400 s gray bar denoting its approximate duration.

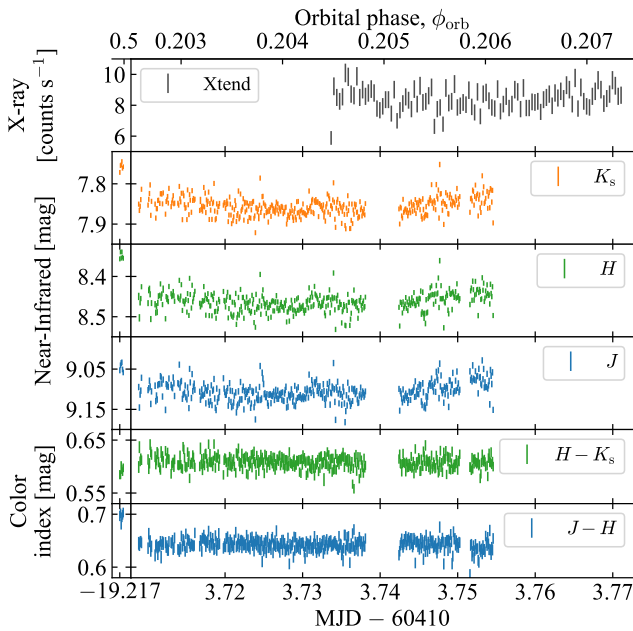


Fig. 8. ksIRIUS and XRISM/Xtend light curves in 2024. From top to bottom, the panels show the XRISM/Xtend light curve (2–10 keV, 32 s bins), the K_s , H , and J bands, and the color indices $H - K_s$ and $J - H$ from ksIRIUS. For the ksIRIUS panels, the left and right columns correspond to the observations on March 21 and April 14, respectively.

thermal plasma emission in this band.

To isolate geometrical effects such as the emitting area, we focus on the flux ratio under the assumption that both jets are intrinsically symmetric, so that any intrinsic power variations cancel out in the ratio. In 2024, the blue-to-red flux ratio expected from Doppler beaming was ~ 2 , which can reasonably explain the in-eclipse data but not the out-of-eclipse phase. In contrast, in 2025 the predicted ratio was close to unity, consistent with the observed values. For a companion size on the order of the disk scale (e.g., Burenin et al. 2011), such partial obscuration of the inner jet regions is plausible. These results support a geometrical interpretation in which the larger line widths of the Fe and Ni emission arise from inner jet regions that are partially obscured by the ac-

cretion disk and the companion star.

4.4 Observed jet angles and velocities

The observed Doppler shifts (figure 5) can be used to investigate the kinematic properties of the jets, such as their ejection direction and velocity. We assume that the blue and red jets are launched simultaneously in opposite directions, at symmetric angles, and share the same intrinsic speed (Marshall et al. 2002).

Under this assumption, the Doppler shifts of the blue and red jets are expressed as

$$\begin{aligned} z_b &= \gamma_{\text{sym}} (1 - \beta_{\text{sym}} \cos \alpha_{\text{sym}}) - 1, \\ z_r &= \gamma_{\text{sym}} (1 + \beta_{\text{sym}} \cos \alpha_{\text{sym}}) - 1, \end{aligned} \quad (2)$$

where α_{sym} and β_{sym} denote the jet angle and speed under the symmetric assumption, and $\gamma_{\text{sym}} = (1 - \beta_{\text{sym}}^2)^{-1/2}$. From equation (2), the apparent jet angle and velocity can then be derived as

$$\begin{aligned} \cos \alpha_{\text{sym}} &= \frac{z_r - z_b}{2 \left(1 + \frac{z_b + z_r}{2}\right) \sqrt{1 - \left(1 + \frac{z_b + z_r}{2}\right)^{-2}}}, \\ \beta_{\text{sym}} &= \sqrt{1 - \left(1 + \frac{z_b + z_r}{2}\right)^{-2}}. \end{aligned} \quad (3)$$

Figure 12 shows the derived α_{sym} and β_{sym} , calculated from the Doppler shifts measured in the Resolve and optical data (figure 5). The Resolve measurements display a clear periodic modulation. The jet angle α_{sym} follows the variation expected from the precession phase, with values of $\sim 70^\circ$ in 2024 (near face-on) and $\sim 90^\circ$ in 2025 (near edge-on), with additional variations attributable to nutation also being visible. The jet velocity β_{sym} shows pronounced variations, ranging from $0.25c$ – $0.28c$ in 2024 and from $0.29c$ – $0.30c$ in 2025. These variations seem periodic, with a timescale comparable to that of nutation.

To quantify this apparent periodicity in β_{sym} , we fit a simple sinusoid with a $-\pi/2$ phase offset, motivated by the observation that the modulation of β_{sym} appears shifted by about -90° relative to the nutation-phase variation of α_{sym} :

$$\beta_{\text{sym,model}} = C_{\text{sym}} + \delta\beta_{\text{sym}} \sin\left(2\pi\phi_{\text{nut}} - \frac{\pi}{2}\right), \quad (4)$$

where C_{sym} is the mean velocity and $\delta\beta_{\text{sym}}$ the modulation amplitude. The nutation period was fixed to the value from Davydon

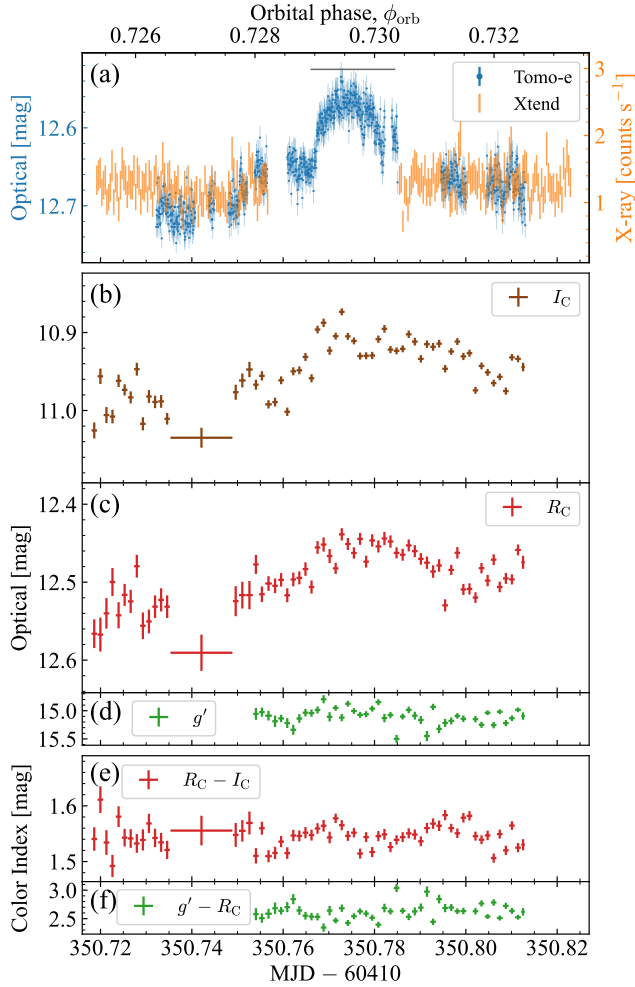


Fig. 9. Light curves with Tomo-e Gozen, XRISM/Xtend, and MITSuME obtained in 2025. (a) Light curve from March 26, showing optical data from Tomo-e Gozen (blue) and X-ray data from XRISM/Xtend (orange; 2–10 keV, 32 s bins). A gray bar with a width of 1600 s indicates the approximate duration of the optical flare. (b)–(d) show MITSuME light curves in the I_C , R_C , and g' bands. (e) and (f) show the color indices calculated as $R_C - I_C$ and $g' - R_C$, respectively.

et al. (2008), and fits were performed separately for 2024 and 2025 due to the large difference in C_{sym} . The best-fit parameters from the Resolve data are summarized in table 2 and shown as solid lines in figures 12c and 12d.

Table 2. Fit results for the apparent jet velocity model in equation (4), corresponding to the curves shown in Figure 12.

Parameter	2024	2025
$t_{0,\text{nut}}$	43032.97 ± 0.02	43033.41 ± 0.20
C_{sym}	0.2646 ± 0.0002	0.2962 ± 0.0031
$\delta\beta_{\text{sym}}$	0.0148 ± 0.0003	0.0075 ± 0.0035

Figures 12c and 12d indicate modulations in the jet speed $\delta\beta_{\text{sym}}$ on a timescale of ~ 6.3 d, comparable to the nutation period. From table 2, they fluctuate around $\sim 0.26 \pm 0.01c$ in 2024 and $\sim 0.30 \pm 0.01c$ in 2025, with a phase offset of about -90° relative to the nutation cycle. These results indicate day-scale modulations as well as a modest year-scale increase in the jet speed between the

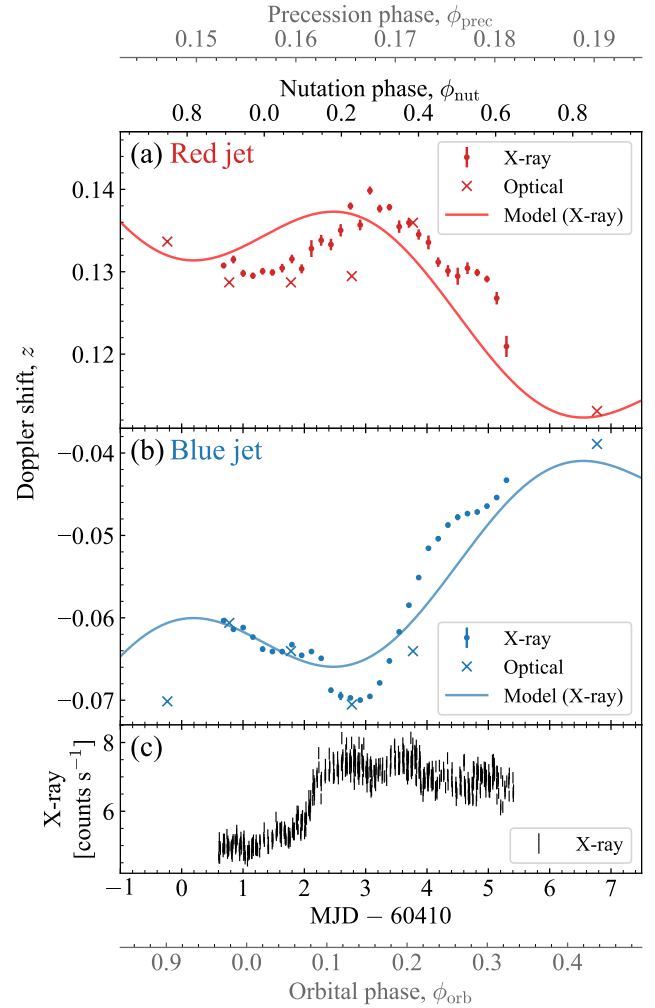


Fig. 10. (a, b) Close-up views of figure 5a, focusing on the 2024 data. The same symbols and line styles are used as in the original figure. (c) XRISM/Xtend light curve in the 2–10 keV band.

two campaigns.

Jet speeds have been reported to vary on multiple timescales. In the optical band, variations on timescales comparable to the orbital period (~ 13.1 d) with amplitudes of $\sim 0.02c$ have been observed (e.g., Blundell et al. 2007). At radio wavelengths, changes over several tens of days reaching up to $\sim 0.3c$ have been reported (e.g., Blundell et al. 2011; Jeffrey et al. 2016), sometimes accompanied by enhanced radio and optical emission. The variations observed with Resolve are comparable in amplitude to these earlier results but occur on shorter timescales of ~ 6.3 d. The higher velocity detected in 2025, reaching $\sim 0.3c$, may be related to the scenario suggested by Blundell et al. (2011), as our optical observations in 2025 showed relatively high fluxes (see subsection 4.1). We note, however, that no contemporaneous radio monitoring was conducted during our campaign, and thus a direct correlation between optical brightness and radio activity could not be evaluated in this work.

The new Resolve measurements show that the jet velocity varies on timescales comparable to nutation, highlighting that the physical mechanism driving these modulations is still not well understood. The fundamental nature of SS 433’s baryonic jets—whether they form a continuous stream or consist of discrete, blob-

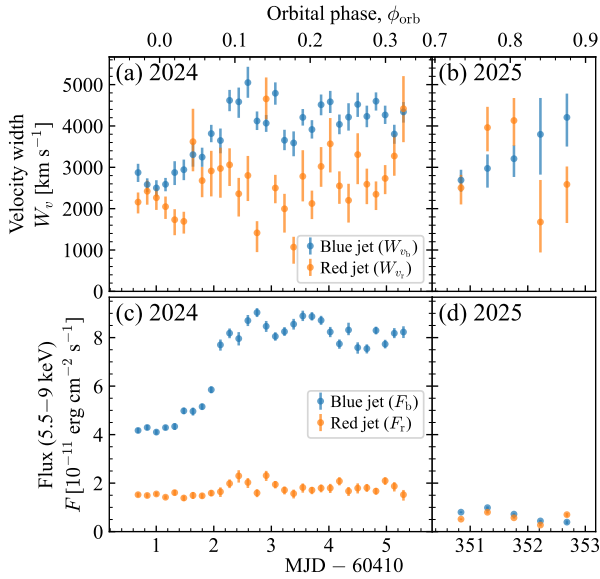


Fig. 11. X-ray jet velocity widths and fluxes derived from Resolve spectral fitting. (a, b) Velocity widths (FWHM; W_v) of the blue ($W_{v,b}$) and red ($W_{v,r}$) jets obtained from the Resolve spectra in the 5.5–9 keV band for 2024 and 2025, respectively (see also Shidatsu et al. (2025) for details of the jet velocity width). (c, d) Fluxes of the blue (F_b) and red (F_r) jets in the same energy band and epochs.

like ejecta—remains uncertain, and it is not yet clear whether the two jets are truly symmetric or share identical velocities. In this analysis, our modeling assumes symmetric jets with equal speeds; however, this simplification may not fully represent the intrinsic dynamics of the system. Interpreting the observed modulations may therefore require considering possible intrinsic asymmetries or time-variable jet speeds linked to the jet-launching physics. Polarization studies in the radio (e.g., Miller-Jones et al. 2008) and X-ray bands (e.g., Kaaret et al. 2024) suggest that magnetic fields tend to align with the jet axis, although the symmetry between the jet and counter-jet may not be perfect. In a super-Eddington accretion regime, radiation pressure and magnetic fields likely interact to shape both the stability and symmetry of the outflows. Since SS 433’s jets evolve under the combined influence of velocity and density contrasts, gravity, radiation, and magnetic stresses, long-term, multi-wavelength, and phase-resolved observations will be essential to determine whether these modulations are periodic and to clarify the physical processes that drive relativistic outflows.

5 Conclusion

We have presented results from XRISM’s coordinated multiwavelength campaign of SS 433, conducted in April 2024 and March 2025, together with optical and near-infrared observations. The XRISM exposures were ~ 200 ks in 2024 and ~ 100 ks in 2025, covering distinct orbital and precessional configurations: in 2024 the approaching jet was inclined toward the observer, while in 2025 the jet axis was nearly perpendicular to the line of sight.

The key advancement from these campaigns comes from time-resolved Doppler-shift measurements with XRISM/Resolve. Resolve’s high spectral resolution and effective area enabled precise separation of numerous emission lines and substantially improved Doppler-shift accuracy compared with earlier studies.

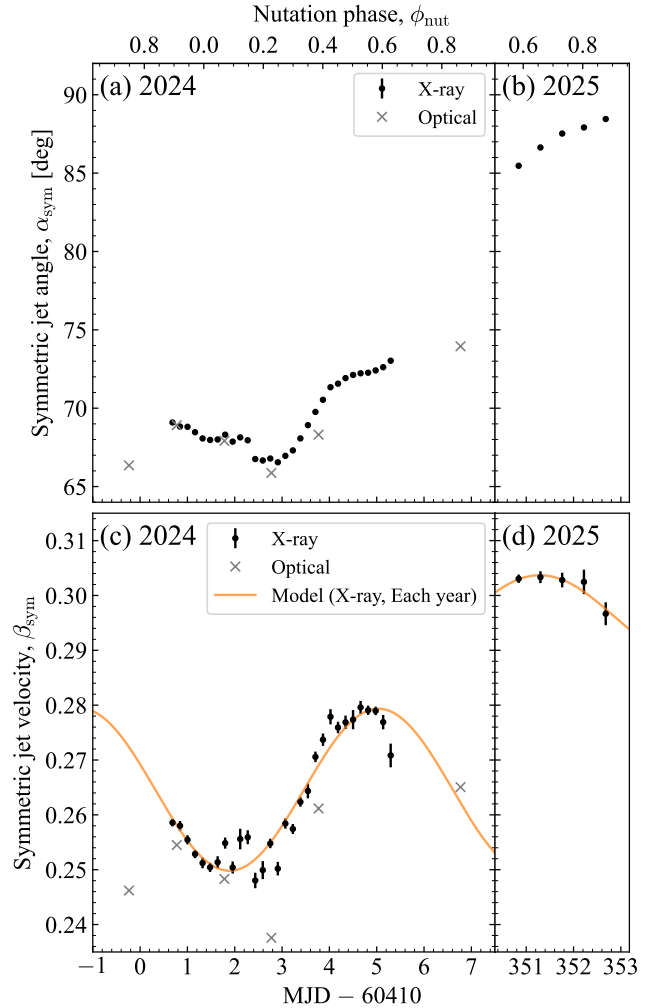


Fig. 12. Jet angles (α_{sym} ; panels a and b) and jet velocities (β_{sym} ; panels c and d) derived under the symmetric assumption (equation (3)) for the years 2024 and 2025. Black points and gray crosses indicate the observed blueshifted and redshifted components obtained with Resolve and Seimei, respectively. Solid lines in panels c and d show the best-fit sinusoidal models described by equation (4), with all parameters fitted independently for each year as listed in table 2.

Simultaneous optical spectroscopy suggested a tendency for the optical emission to lag slightly behind the X-rays. Resolve revealed an asymmetry between the two jet components, with velocities of $\sim 0.26c$ in 2024 and $\sim 0.30c$ in 2025, showing sinusoidal modulations with amplitudes $\sim \pm 0.01c$. These variations follow the 6.3-d nutation period but are offset in phase by about -90° , suggesting a possible connection between nutation and jet-velocity fluctuations. These results likely reflect changes in viewing geometry between the two epochs, which affected how the inner jet regions were seen. The blue jet in 2024, observed during the out-of-eclipse phase, showed a larger velocity width than the red jet, whereas in 2025 both jets showed comparable widths. The jet brightness also followed this geometrical trend, consistent with the interpretation by Shidatsu et al. (2025) that the line widths increase toward the inner regions of the jet.

Optical photometry detected short flares of ~ 400 s in 2024 and ~ 1600 s in 2025, with amplitudes up to $\sim 15\%$ during out-of-eclipse intervals. X-ray variability was not detected within the

statistical limits and within the limited duration of the simultaneous observations. Near-infrared observations with kSIRIUS in 2024 did not show significant variability, consistent with the X-ray data. The optical flux in 2025 was higher by ~ 0.1 mag relative to 2024 at comparable orbital phases, while the color indices remained consistent across the two epochs. Continued long-term monitoring across a broader range of orbital, precessional, and nutation phases—with XRISM and complementary multiwavelength observations—will be essential for disentangling these effects and refining our understanding of the dynamical properties of the relativistic jets in SS 433.

Funding

D.H. acknowledges support from NASA grant HST-GO-17770.002-A. This work was also supported by the U.S. National Science Foundation (NSF) under Cooperative Agreement PHY-2019786 (The NSF AI Institute for Artificial Intelligence and Fundamental Interactions, <http://iaifi.org/>). K.O. acknowledges support from the Korea Astronomy and Space Science Institute under the R&D program (Project No. 2026-1-831-01), supervised by the Korea AeroSpace Administration, and from the National Research Foundation of Korea (NRF) grant funded by the Korea government (MSIT) (RS-2025-00553982). Additional support was provided by JSPS KAKENHI Grant Numbers 24KJ2067 (Y.S.), 19K14762, 23K03459, 24H01812 (M.S.), 20H01946 (Y.U.), 22H01272, 23K22543, 24K00672 (M.M.), 22K20386 (H.S.), 24H00248, 24K00680, and 25K01041 (K.N.).

Acknowledgments

We thank all colleagues involved in the coordinated multiwavelength campaign, including the teams of the XRISM, Seimei, LCO, Tomo-e Gozen, MITSuME, and kSIRIUS, for their complementary observations and support. M.S., T.T., T.U., M.U., and M.Y. acknowledge support by Ehime University Grant-in-Aid Research Empowerment Program. The 3.8 m Seimei Telescope observations were carried out through programs 24A-N-CT07 (NAOJ open use) and 24A-K-0015 (Kyoto University time). We are grateful to the graduate and undergraduate students who conducted near-infrared observations of kSIRIUS using the 1-m Kagoshima telescope at Iriki Observatory. This work was partially supported by the joint research program of the Institute for Cosmic Ray Research (ICRR), the University of Tokyo. The Seimei telescope at the Okayama Observatory is jointly operated by Kyoto University and the National Astronomical Observatory of Japan (NAOJ), with assistance provided by the OISTER program. The Kagoshima University 1 m telescope and the MITSuME 50 cm telescopes at Akeno and Okayama are members of the OISTER program, funded by MEXT of Japan.

We further acknowledge the use of public data and services from the High Energy Astrophysics Science Archive Research Center (HEASARC) at NASA/GSFC, and the astrometric calibration tools provided by WCS coordinate routines and the open-source project Astrometry.net (<https://astrometry.net/>) (Lang et al. 2010). We thank the developers for making these resources freely available to the community. We also thank the referee for constructive and helpful comments that improved the clarity of the manuscript.

Appendix 1 Tomo-e Gozen field of view and photometric aperture

This appendix presents the field of view and photometric aperture used in the Tomo-e Gozen analysis. Figure 13 shows the observation from 2024 April 10, highlighting SS 433 and the calibration stars. This image illustrates the aperture placement and source isolation, supporting the calibration procedure described in subsection 2.4.

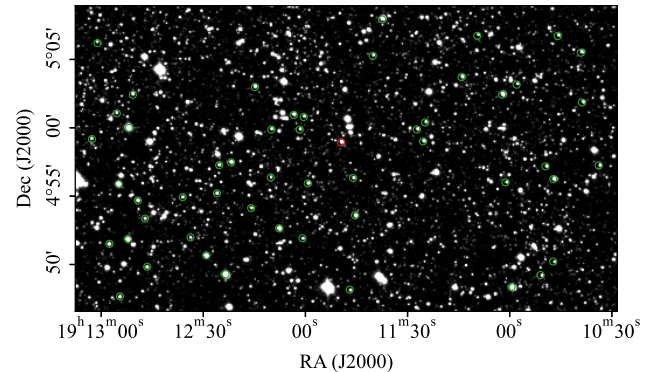


Fig. 13. Full-field optical image of the SS 433 region obtained with Tomo-e Gozen. The image corresponds to the first data cube acquired on 2024 April 10 and is generated by stacking 10 consecutive frames with background subtraction applied. SS 433 and the photometric calibration stars are indicated by red and green circles, respectively. All markers have a radius of 13 pixels ($\sim 15''$), matching the photometric aperture used in the analysis.

Appendix 2 Color index diagrams

Color–magnitude and color–color diagrams are commonly used to examine the variability of astrophysical sources (e.g., Bessell & Brett 1988). Here we present such diagrams derived from MITSuME and kSIRIUS photometric data for reference.

Figure 15 shows the MITSuME color–magnitude and color–color diagrams, derived from figures 14 and 9. Figure 16 presents the near-infrared diagrams from the kSIRIUS data shown in figure 8. Some optical panels appear to show weak trends between color and magnitude, whereas the near-infrared diagrams do not exhibit any obvious pattern.

Appendix 3 Full-band spectrum of XRISM/Resolve

For reference, we show the full-band (1.7–10 keV) XRISM/Resolve spectra. Figure 17 displays the data for the same time intervals as in subsection 3.1, showing emission lines from lighter elements such as Si and S in the soft X-ray band (see also Shidatsu et al. 2025).

References

- Abell, G. O., & Margon, B. 1979, *Nature*, 279, 701
- Arnaud, K. A. 1996, in *Astronomical Society of the Pacific Conference Series*, Vol. 101, *Astronomical Data Analysis Software and Systems V*, ed. G. H. Jacoby & J. Barnes, 17

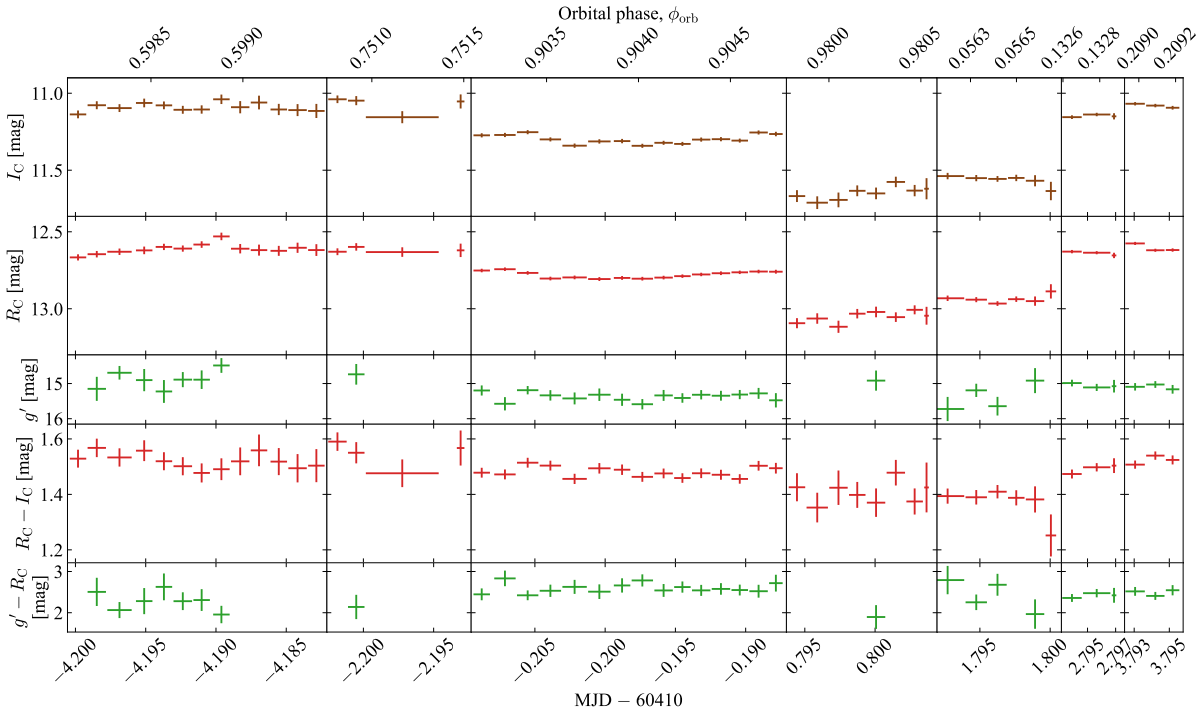


Fig. 14. Light curves obtained with MITSuME during April 5–13, 2024. From top to bottom, the panels show the I_C , R_C , g' bands, followed by the color indices $R_C - I_C$ and $g' - R_C$.

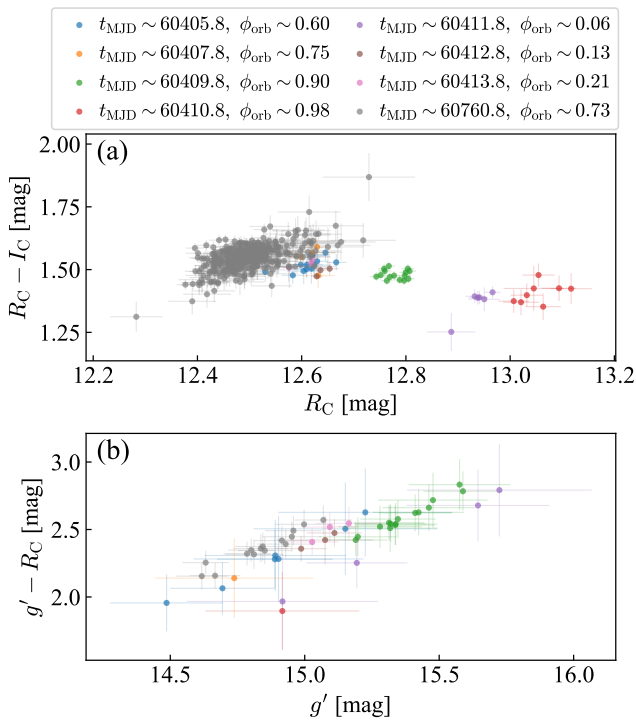


Fig. 15. Scatter plots of magnitude versus color index based on the MITSuME light curve data shown in figure 14 (2024) and figure 9 (2025). Panel (a) shows R_C versus $R_C - I_C$, and panel (b) shows g' versus $g' - R_C$.

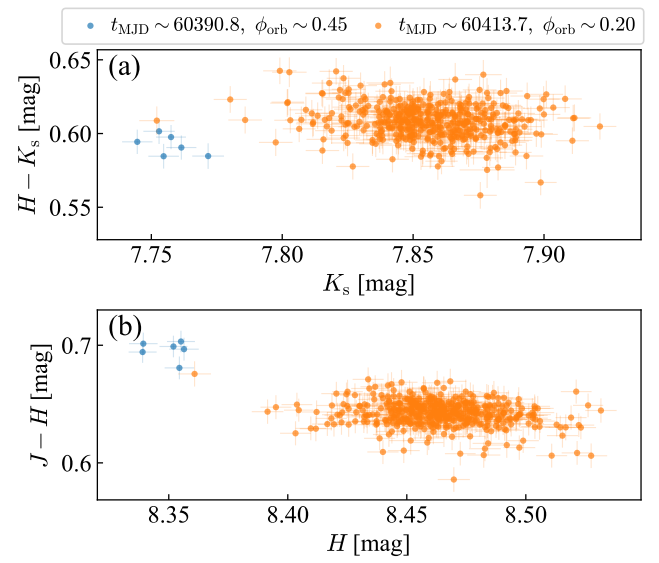


Fig. 16. Scatter plots of magnitude versus color index based on the kSIR-IUS light curve data shown in figure 8. Panel (a) shows K_s versus $H - K_s$, and panel (b) shows H versus $J - H$.

Table 3. Doppler shifts from the time-resolved Resolve spectra, fitted with a thermal model (see figure 3).

ID	MJD _{mid}	Exposure (s)	z_b	$W_{v_b}^*$ (10^3)	N_b^\dagger (10^1)	z_r	$W_{v_r}^*$ (10^3)	N_r^\dagger (10^1)
2024								
0	60410.684	7995	-0.0603 ± 0.0003	$2.9^{+0.4}_{-0.3}$	0.87 ± 0.07	0.1308 ± 0.0006	$2.2^{+0.5}_{-0.4}$	0.48 ± 0.05
1	60410.843	8130	$-0.0614^{+0.0004}_{-0.0002}$	$2.6^{+0.3}_{-0.2}$	0.85 ± 0.07	$0.1315^{+0.0008}_{-0.0007}$	$2.4^{+0.5}_{-0.4}$	0.45 ± 0.04
2	60411.002	7921	-0.0612 ± 0.0003	2.5 ± 0.3	$0.78^{+0.07}_{-0.06}$	0.1298 ± 0.0007	$2.3^{+0.5}_{-0.4}$	0.44 ± 0.04
3	60411.161	9192	-0.0623 ± 0.0003	2.6 ± 0.3	0.86 ± 0.06	$0.1295^{+0.0007}_{-0.0006}$	$2.0^{+0.5}_{-0.4}$	0.43 ± 0.04
4	60411.320	4684	$-0.0638^{+0.0006}_{-0.0005}$	2.9 ± 0.5	$0.77^{+0.08}_{-0.07}$	$0.1301^{+0.0007}_{-0.0006}$	$1.7^{+0.6}_{-0.4}$	0.43 ± 0.05
5	60411.479	5600	-0.0641 ± 0.0004	2.9 ± 0.4	$1.00^{+0.09}_{-0.08}$	$0.1299^{+0.0007}_{-0.0006}$	$1.7^{+0.5}_{-0.4}$	$0.42^{+0.06}_{-0.05}$
6	60411.638	6230	-0.0641 ± 0.0005	3.3 ± 0.5	$0.98^{+0.13}_{-0.09}$	$0.1304^{+0.0008}_{-0.0009}$	$3.6^{+1.2}_{-1.3}$	$0.46^{+0.07}_{-0.06}$
7	60411.797	7449	-0.0633 ± 0.0004	3.2 ± 0.4	$0.98^{+0.07}_{-0.06}$	0.1315 ± 0.0009	$2.7^{+0.7}_{-0.5}$	0.42 ± 0.05
8	60411.956	9239	$-0.0645^{+0.0004}_{-0.0005}$	3.8 ± 0.3	1.10 ± 0.07	$0.1304^{+0.0008}_{-0.0009}$	$2.9^{+1.0}_{-0.8}$	0.45 ± 0.05
9	60412.115	4097	-0.0641 ± 0.0005	3.6 ± 0.5	1.47 ± 0.12	$0.1328^{+0.0016}_{-0.0017}$	$3.0^{+1.2}_{-0.8}$	0.47 ± 0.09
10	60412.274	6982	-0.0649 ± 0.0005	4.6 ± 0.4	1.57 ± 0.11	0.1338 ± 0.0011	$3.1^{+0.8}_{-0.7}$	0.58 ± 0.08
11	60412.433	4455	$-0.0688^{+0.0006}_{-0.0005}$	4.6 ± 0.6	$1.43^{+0.13}_{-0.12}$	$0.1333^{+0.0012}_{-0.0011}$	$2.4^{+0.9}_{-0.6}$	0.62 ± 0.10
12	60412.592	5285	$-0.0695^{+0.0009}_{-0.0008}$	5.0 ± 0.6	$1.60^{+0.12}_{-0.11}$	$0.1350^{+0.0012}_{-0.0013}$	$2.8^{+1.0}_{-0.8}$	0.56 ± 0.09
13	60412.751	8682	$-0.0697^{+0.0003}_{-0.0005}$	4.1 ± 0.4	1.72 ± 0.09	0.1380 ± 0.0007	$1.4^{+0.8}_{-0.5}$	0.46 ± 0.07
14	60412.910	8121	$-0.0700^{+0.0003}_{-0.0004}$	4.1 ± 0.3	$1.55^{+0.09}_{-0.08}$	$0.1357^{+0.0008}_{-0.0013}$	$4.7^{+0.8}_{-0.9}$	0.65 ± 0.07
15	60413.069	8179	$-0.0695^{+0.0004}_{-0.0003}$	$4.8^{+0.5}_{-0.4}$	1.54 ± 0.09	0.1399 ± 0.0008	$2.5^{+0.6}_{-0.5}$	0.58 ± 0.07
16	60413.228	7401	$-0.0679^{+0.0003}_{-0.0004}$	3.7 ± 0.4	$1.69^{+0.11}_{-0.10}$	$0.1377^{+0.0007}_{-0.0008}$	$2.0^{+0.9}_{-0.6}$	0.54 ± 0.08
17	60413.387	3884	-0.0652 ± 0.0005	3.6 ± 0.5	$1.72^{+0.14}_{-0.12}$	$0.1378^{+0.0007}_{-0.0006}$	$1.1^{+0.7}_{-0.4}$	0.48 ± 0.09
18	60413.546	6527	$-0.0617^{+0.0003}_{-0.0004}$	4.2 ± 0.3	$1.65^{+0.12}_{-0.11}$	$0.1355^{+0.0013}_{-0.0012}$	2.8 ± 1.0	0.51 ± 0.08
19	60413.705	7132	$-0.0585^{+0.0003}_{-0.0004}$	3.9 ± 0.4	$1.75^{+0.10}_{-0.09}$	0.1360 ± 0.0009	$2.1^{+0.6}_{-0.5}$	0.50 ± 0.07
20	60413.864	7067	-0.0551 ± 0.0005	4.5 ± 0.4	$1.69^{+0.11}_{-0.09}$	$0.1345^{+0.0011}_{-0.0010}$	3.0 ± 0.8	0.51 ± 0.07
21	60414.023	6388	$-0.0516^{+0.0003}_{-0.0004}$	4.6 ± 0.4	$1.66^{+0.12}_{-0.11}$	0.1336 ± 0.0014	$3.6^{+1.1}_{-1.0}$	$0.53^{+0.09}_{-0.08}$
22	60414.182	6528	-0.0504 ± 0.0005	4.0 ± 0.4	1.52 ± 0.10	$0.1312^{+0.0010}_{-0.0009}$	$2.6^{+0.7}_{-0.6}$	0.59 ± 0.08
23	60414.341	5523	-0.0487 ± 0.0005	$4.2^{+0.5}_{-0.6}$	$1.66^{+0.12}_{-0.11}$	$0.1301^{+0.0011}_{-0.0012}$	$2.2^{+0.9}_{-0.7}$	0.48 ± 0.08
24	60414.500	4872	-0.0478 ± 0.0006	4.5 ± 0.5	1.47 ± 0.12	$0.1295^{+0.0018}_{-0.0016}$	$3.3^{+1.2}_{-0.9}$	0.50 ± 0.09
25	60414.659	6164	-0.0474 ± 0.0004	4.2 ± 0.4	$1.64^{+0.14}_{-0.11}$	$0.1304^{+0.0012}_{-0.0011}$	$2.6^{+0.8}_{-0.6}$	0.58 ± 0.08
26	60414.818	9222	$-0.0472^{+0.0004}_{-0.0005}$	4.6 ± 0.4	1.67 ± 0.09	0.1299 ± 0.0007	$2.3^{+0.6}_{-0.5}$	0.49 ± 0.06
27	60414.977	8022	$-0.0464^{+0.0004}_{-0.0005}$	4.3 ± 0.4	$1.48^{+0.09}_{-0.08}$	$0.1291^{+0.0007}_{-0.0006}$	$2.7^{+0.6}_{-0.5}$	0.57 ± 0.07
28	60415.136	8045	-0.0454 ± 0.0005	3.8 ± 0.4	$1.69^{+0.12}_{-0.11}$	$0.1268^{+0.0012}_{-0.0013}$	$3.3^{+0.8}_{-0.9}$	$0.55^{+0.08}_{-0.09}$
29	60415.295	5312	-0.0433 ± 0.0004	4.3 ± 0.4	$1.72^{+0.14}_{-0.15}$	$0.1209^{+0.0026}_{-0.0016}$	4.4 ± 1.3	$0.44^{+0.10}_{-0.09}$
2025								
0	60760.840	23163	0.0242 ± 0.0005	$2.7^{+0.5}_{-0.4}$	$0.19^{+0.03}_{-0.02}$	0.0745 ± 0.0007	$2.5^{+0.7}_{-0.5}$	$0.13^{+0.02}_{-0.01}$
1	60761.300	16193	0.0308 ± 0.0006	$3.0^{+0.8}_{-0.6}$	$0.23^{+0.04}_{-0.03}$	$0.0681^{+0.0010}_{-0.0011}$	$4.0^{+0.9}_{-0.8}$	0.20 ± 0.02
2	60761.760	22468	$0.0355^{+0.0008}_{-0.0007}$	$3.2^{+0.7}_{-0.5}$	$0.17^{+0.03}_{-0.02}$	$0.0630^{+0.0013}_{-0.0014}$	$4.1^{+1.0}_{-0.9}$	0.14 ± 0.02
3	60762.220	15005	$0.0376^{+0.0021}_{-0.0020}$	$3.8^{+1.6}_{-1.5}$	0.11 ± 0.02	$0.0607^{+0.0016}_{-0.0015}$	$1.7^{+1.2}_{-1.7}$	0.07 ± 0.02
4	60762.680	21543	$0.0388^{+0.0018}_{-0.0016}$	$4.2^{+1.2}_{-0.9}$	0.17 ± 0.03	$0.0555^{+0.0016}_{-0.0017}$	$2.6^{+1.5}_{-0.7}$	0.10 ± 0.03

Subscripts b and r denote the blue and red jet components, respectively. Uncertainties are at the 90% confidence level.

* W_v denotes the velocity width (FWHM) in km s^{-1} .

† N is the normalization as defined in XSPEC.

‡ kT is in keV.

§ Abundances relative to the solar value (Lodders et al. 2009).

|| N_{gau} is in units of photons $\text{cm}^{-2} \text{s}^{-1}$.

F is in $\text{erg cm}^{-2} \text{s}^{-1}$.

Brinkmann, W., Kawai, N., Matsuoka, M., & Fink, H. H. 1991, *A&A*, 241, 112

Brown, T. M., Baliber, N., Bianco, F. B., et al. 2013, *PASP*, 125, 1031

Burenin, R. A., Revnivtsev, M. G., Khamitov, I. M., et al. 2011, *Astronomy Letters*, 37, 100

Chambers, K. C., Magnier, E. A., Metcalfe, N., et al. 2016, arXiv e-prints, arXiv:1612.05560

Cherepashchuk, A., Belinski, A., Dodin, A., & Postnov, K. 2023, *New Astronomy*, 103, 102060

Cherepashchuk, A. M., Belinski, A. A., Dodin, A. V., & Postnov, K. A. 2021, *MNRAS*, 507, L19

Cherepashchuk, A. M., Dodin, A. V., & Postnov, K. A. 2025, arXiv e-prints, arXiv:2506.01106

Cherepashchuk, A. M., Dodin, A. V., Postnov, K. A., et al. 2022, *Astronomy Reports*, 66, 451

Cherepashchuk, A. M., Esipov, V. F., Dodin, A. V., Davydov, V. V., & Belinskii, A. A. 2018, *Astronomy Reports*, 62, 747

Cherepashchuk, A. M., Sunyaev, R. A., Fabrika, S. N., et al. 2005, *A&A*, 437, 561

Collins, G. W., & Scher, R. W. 2002, *MNRAS*, 336, 1011

Collins, II, G. W., & Newsom, G. H. 1988, *ApJ*, 331, 486

Crampton, D., & Hutchings, J. B. 1981, *ApJ*, 251, 604

Cutri, R. M., Skrutskie, M. F., van Dyk, S., et al. 2003, *VizieR Online Data Catalog: 2MASS All-Sky Catalog of Point Sources (Cutri+ 2003)*, *VizieR On-line Data Catalog: II/246*. Originally published in: University of Massachusetts and Infrared Processing and Analysis

Table 3 (continued). Global parameters, flux, and fit quality.

ID	kT^\ddagger	A_{Fe}^\S	A_{Ni}^\S	N_{gau}^\parallel	$F_{\text{b}}^\# (10^{-11})$	$F_{\text{r}}^\# (10^{-11})$	$F_{\text{all}}^{(\text{abs})\#} (10^{-11})$	$\chi^2/\text{d.o.f.}$
2024								
0	5.9 ± 0.3	$1.01^{+0.11}_{-0.10}$	$8.4^{+1.2}_{-1.1}$	3.9 ± 1.3	4.17 ± 0.17	1.52 ± 0.14	5.56 ± 0.12	398/402
1	$6.3^{+0.4}_{-0.3}$	$1.06^{+0.12}_{-0.10}$	$8.9^{+1.3}_{-1.1}$	4.4 ± 1.4	4.29 ± 0.17	$1.49^{+0.15}_{-0.14}$	5.65 ± 0.12	449/411
2	$6.5^{+0.3}_{-0.4}$	$1.12^{+0.13}_{-0.12}$	$9.8^{+1.4}_{-1.3}$	5.1 ± 1.5	4.10 ± 0.17	1.55 ± 0.14	5.54 ± 0.12	387/397
3	6.3 ± 0.3	$1.03^{+0.10}_{-0.09}$	$8.7^{+1.2}_{-1.1}$	5.0 ± 1.3	4.29 ± 0.16	1.42 ± 0.13	5.59 ± 0.11	449/455
4	$7.0^{+0.4}_{-0.5}$	$1.20^{+0.17}_{-0.16}$	$10.5^{+2.0}_{-1.8}$	6.0 ± 2.0	4.34 ± 0.23	1.61 ± 0.19	5.83 ± 0.16	269/258
5	6.4 ± 0.4	$1.01^{+0.12}_{-0.11}$	$6.9^{+1.3}_{-1.2}$	6.9 ± 1.9	4.98 ± 0.22	1.39 ± 0.18	6.24 ± 0.15	336/326
6	$6.5^{+0.4}_{-0.5}$	$0.93^{+0.13}_{-0.14}$	8.6 ± 1.6	7.0 ± 1.9	$4.96^{+0.26}_{-0.28}$	$1.49^{+0.25}_{-0.23}$	$6.34^{+0.14}_{-0.15}$	430/369
7	6.8 ± 0.3	1.07 ± 0.11	8.0 ± 1.2	6.1 ± 1.6	5.15 ± 0.21	1.48 ± 0.17	6.49 ± 0.13	470/439
8	7.1 ± 0.3	1.05 ± 0.10	$7.8^{+1.2}_{-1.1}$	7.1 ± 1.6	5.85 ± 0.23	1.59 ± 0.20	7.29 ± 0.12	660/583
9	7.2 ± 0.4	$0.93^{+0.12}_{-0.11}$	$8.1^{+1.6}_{-1.4}$	11.1 ± 2.8	$7.70^{+0.37}_{-0.38}$	$1.64^{+0.33}_{-0.32}$	9.17 ± 0.21	406/355
10	7.5 ± 0.4	$0.91^{+0.10}_{-0.09}$	$6.3^{+1.1}_{-1.0}$	11.0 ± 2.2	$8.18^{+0.33}_{-0.34}$	$1.98^{+0.30}_{-0.29}$	9.97 ± 0.17	642/608
11	8.5 ± 0.6	$0.89^{+0.13}_{-0.11}$	$8.0^{+1.7}_{-1.6}$	9.7 ± 2.7	7.96 ± 0.45	$2.30^{+0.42}_{-0.41}$	10.04 ± 0.21	481/423
12	7.9 ± 0.5	1.01 ± 0.12	$5.6^{+1.3}_{-1.2}$	$10.8^{+2.5}_{-2.6}$	$8.70^{+0.39}_{-0.37}$	$2.03^{+0.32}_{-0.34}$	10.51 ± 0.20	561/511
13	8.1 ± 0.4	0.87 ± 0.08	$4.5^{+0.9}_{-0.8}$	10.4 ± 2.0	9.04 ± 0.30	$1.59^{+0.27}_{-0.26}$	10.41 ± 0.15	821/732
14	7.9 ± 0.3	0.94 ± 0.07	7.5 ± 0.9	$11.3^{+2.0}_{-2.1}$	$8.47^{+0.37}_{-0.38}$	2.31 ± 0.34	10.56 ± 0.16	743/708
15	$7.5^{+0.4}_{-0.3}$	$0.89^{+0.09}_{-0.08}$	$6.2^{+1.0}_{-0.9}$	7.8 ± 1.8	8.05 ± 0.29	1.94 ± 0.25	9.77 ± 0.15	728/676
16	$7.1^{+0.3}_{-0.4}$	0.78 ± 0.08	4.8 ± 0.8	11.8 ± 2.2	$8.25^{+0.31}_{-0.29}$	$1.71^{+0.25}_{-0.27}$	9.77 ± 0.16	719/627
17	7.1 ± 0.5	$0.86^{+0.11}_{-0.10}$	$5.6^{+1.2}_{-1.1}$	9.6 ± 2.8	$8.56^{+0.37}_{-0.36}$	1.57 ± 0.30	9.91 ± 0.22	383/363
18	7.6 ± 0.4	1.06 ± 0.11	$6.7^{+1.2}_{-1.1}$	10.5 ± 2.3	$8.89^{+0.37}_{-0.34}$	$1.82^{+0.30}_{-0.32}$	10.49 ± 0.18	705/596
19	7.2 ± 0.3	$0.96^{+0.09}_{-0.08}$	$6.0^{+1.0}_{-0.9}$	15.1 ± 2.4	$8.87^{+0.30}_{-0.27}$	$1.71^{+0.22}_{-0.26}$	10.42 ± 0.17	708/635
20	7.2 ± 0.3	$1.02^{+0.09}_{-0.10}$	7.0 ± 1.0	12.2 ± 2.3	$8.71^{+0.31}_{-0.30}$	$1.79^{+0.26}_{-0.27}$	10.32 ± 0.17	658/622
21	$7.1^{+0.3}_{-0.4}$	0.95 ± 0.10	$6.0^{+1.1}_{-1.0}$	8.9 ± 2.1	8.23 ± 0.35	1.80 ± 0.31	9.82 ± 0.17	560/556
22	7.5 ± 0.4	0.97 ± 0.10	$6.2^{+1.1}_{-0.9}$	9.6 ± 2.1	$7.74^{+0.31}_{-0.33}$	$2.08^{+0.29}_{-0.27}$	9.63 ± 0.17	616/560
23	7.4 ± 0.4	1.00 ± 0.11	5.1 ± 1.0	12.1 ± 2.5	$8.31^{+0.51}_{-0.35}$	1.67 ± 0.30	$9.81^{+0.18}_{-0.19}$	550/492
24	$7.6^{+0.5}_{-0.4}$	$1.07^{+0.14}_{-0.12}$	5.4 ± 1.2	9.4 ± 2.4	$7.59^{+0.37}_{-0.40}$	$1.79^{+0.36}_{-0.33}$	9.20 ± 0.19	416/419
25	$6.6^{+0.3}_{-0.4}$	0.89 ± 0.10	$4.9^{+1.0}_{-0.9}$	10.0 ± 2.2	$7.54^{+0.30}_{-0.32}$	$1.81^{+0.28}_{-0.26}$	9.18 ± 0.17	542/510
26	7.1 ± 0.3	$1.02^{+0.09}_{-0.08}$	6.0 ± 0.8	9.7 ± 1.8	8.29 ± 0.26	1.67 ± 0.23	9.77 ± 0.14	838/718
27	7.6 ± 0.3	1.08 ± 0.10	$6.6^{+1.0}_{-0.9}$	11.4 ± 2.0	$7.73^{+0.30}_{-0.29}$	$2.10^{+0.25}_{-0.26}$	9.65 ± 0.15	718/645
28	7.1 ± 0.3	$0.90^{+0.09}_{-0.08}$	6.1 ± 0.9	11.5 ± 2.1	$8.18^{+0.36}_{-0.33}$	$1.87^{+0.30}_{-0.33}$	9.87 ± 0.15	761/658
29	7.1 ± 0.4	$0.99^{+0.13}_{-0.10}$	$4.4^{+1.1}_{-0.9}$	8.7 ± 2.4	8.23 ± 0.40	1.52 ± 0.36	9.56 ± 0.19	482/464
2025								
0	$6.9^{+0.5}_{-0.6}$	0.99 ± 0.14	$6.6^{+1.3}_{-1.2}$	2.2 ± 0.5	0.80 ± 0.06	0.51 ± 0.06	1.30 ± 0.03	280/287
1	$6.8^{+0.7}_{-0.5}$	$1.20^{+0.20}_{-0.17}$	$6.2^{+1.4}_{-1.3}$	$2.5^{+0.7}_{-0.8}$	0.99 ± 0.09	0.80 ± 0.09	1.76 ± 0.04	263/274
2	6.7 ± 0.5	$1.17^{+0.17}_{-0.16}$	$6.9^{+1.5}_{-1.4}$	$1.7^{+0.6}_{-0.7}$	$0.72^{+0.06}_{-0.07}$	0.57 ± 0.06	1.27 ± 0.03	251/274
3	$8.5^{+1.8}_{-1.3}$	$0.62^{+0.27}_{-0.19}$	$4.8^{+2.5}_{-2.0}$	0.6 ± 0.5	0.44 ± 0.08	$0.27^{+0.08}_{-0.07}$	0.70 ± 0.03	116/98
4	7.1 ± 0.5	$0.99^{+0.16}_{-0.15}$	$5.1^{+1.4}_{-1.3}$	$1.4^{+0.7}_{-0.8}$	$0.39^{+0.13}_{-0.12}$	$0.70^{+0.12}_{-0.13}$	1.07 ± 0.03	224/225

Subscripts b and r denote the blue and red jet components, respectively. Uncertainties are at the 90% confidence level.

* W_v denotes the velocity width (FWHM) in km s^{-1} .

† N is the normalization as defined in XSPEC.

‡ kT is in keV.

§ Abundances relative to the solar value (Lodders et al. 2009).

∥ N_{gau} is in units of photons $\text{cm}^{-2} \text{s}^{-1}$.

F is in $\text{erg cm}^{-2} \text{s}^{-1}$.

Center, (IPAC/California Institute of Technology) (2003)
 Davydov, V. V., Esipov, V. F., & Cherepashchuk, A. M. 2008, *Astronomy Reports*, 52, 487
 Dubner, G. M., Holdaway, M., Goss, W. M., & Mirabel, I. F. 1998, *AJ*, 116, 1842
 Eikenberry, S. S., Cameron, P. B., Fierce, B. W., et al. 2001, *ApJ*, 561, 1027
 Fabrika, S. 2004, *Astrophys. Space Phys. Res.*, 12, 1
 Gaia Collaboration, Vallenari, A., Brown, A. G. A., et al. 2023, *A&A*, 674, A1
 Geldzahler, B. J., Pauls, T., & Salter, C. J. 1980, *A&A*, 84, 237
 Gies, D. R., McSwain, M. V., Riddle, R. L., et al. 2002, *The Astrophysical Journal*, 566, 1069
 Goranskij, V. 2011, *Peremennye Zvezdy*, 31, 5

Hillwig, T. C., Gies, D. R., Huang, W., et al. 2004, *The Astrophysical Journal*, 615, 422
 Hjellming, R. M., & Johnston, K. J. 1981, *ApJL*, 246, L141
 Ishisaki, Y., Kelley, R. L., Awaki, H., et al. 2022, in *Society of Photo-Optical Instrumentation Engineers (SPIE) Conference Series*, Vol. 12181, *Space Telescopes and Instrumentation 2022: Ultraviolet to Gamma Ray*, ed. J.-W. A. den Herder, S. Nikzad, & K. Nakazawa, 121811S
 Jeffrey, R. M., Blundell, K. M., Trushkin, S. A., & Mioduszewski, A. J. 2016, *MNRAS*, 461, 312
 Kaaret, P., Ferrazzoli, R., Silvestri, S., et al. 2024, *ApJL*, 961, L12
 Katz, J. I., Anderson, S. F., Margon, B., & Grandi, S. A. 1982, *ApJ*, 260, 780
 Kayama, K., Tanaka, T., Uchida, H., et al. 2025, *Publications of the Astronomical Society of Japan*, psaf059

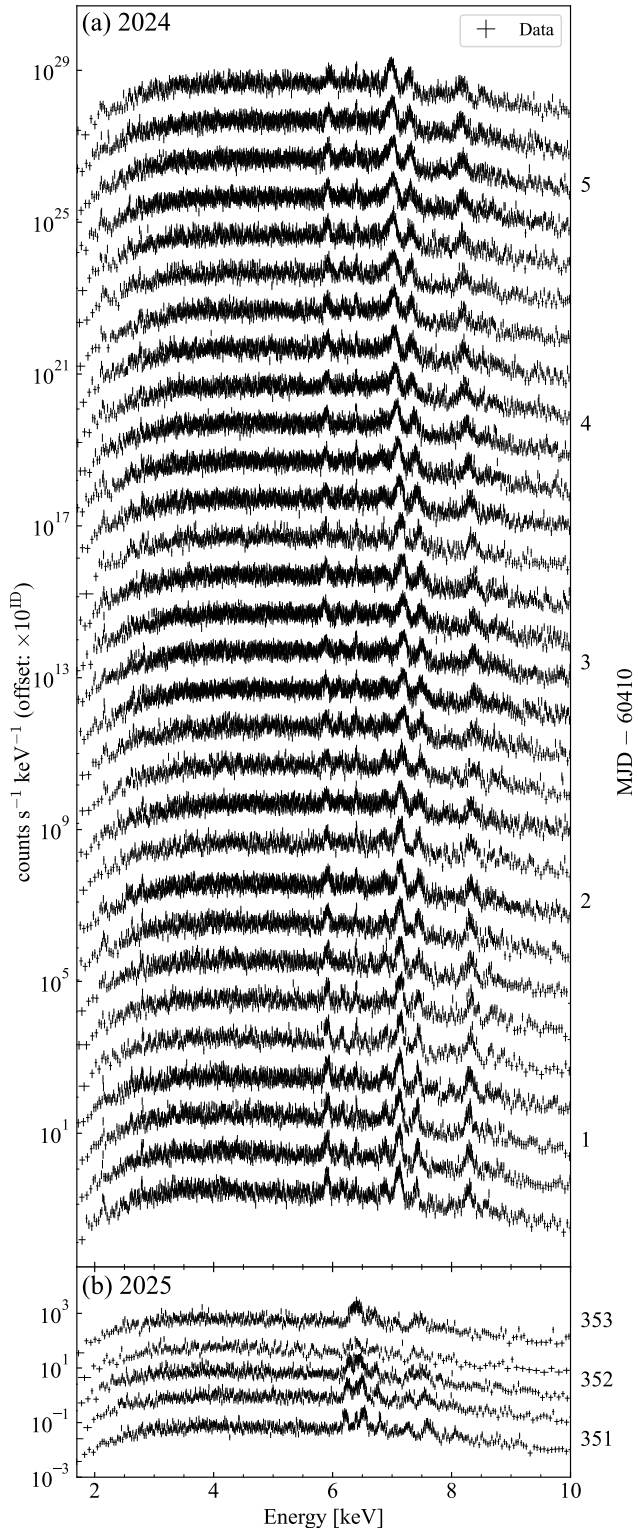


Fig. 17. Time-resolved XRISM/Resolve spectra in the 1.7–10 keV band from 2024 (a) and 2025 (b). Black points represent the observed data, shown with vertical offsets for clarity. The 2024 data are divided into 30 time segments, and the 2025 data into 5 segments.

Kodaira, K., Nakada, Y., & Backman, D. E. 1985, *ApJ*, 296, 232

Kojima, Y., Sako, S., Ohsawa, R., et al. 2018, in *High Energy, Optical, and Infrared Detectors for Astronomy VIII*, ed. A. D. Holland & J. Beletic,

Table 4. Doppler shifts of the $H\alpha$ line from Seimei and LCO observations (see figure 4).

ID	MJD	$H\alpha_b$ [Å]	$H\alpha_r$ [Å]	z_b	z_r
Seimei					
0	60405.8042	6067.50	7525.00	−0.0755	0.1466
1	60406.7875	6017.50	7530.00	−0.0831	0.1474
2	60409.7653	6102.50	7440.00	−0.0701	0.1337
3	60410.7757	6165.00	7407.50	−0.0606	0.1287
4	60411.7812	6142.50	7407.50	−0.0640	0.1287
5	60412.7743	6100.00	7412.50	−0.0705	0.1295
6	60413.7715	6142.50	7455.00	−0.0640	0.1359
7	60416.7715	6307.50	7305.00	−0.0389	0.1131
8	60418.7799	6262.50	7292.50	−0.0458	0.1112
9	60424.7715	6400.00	7165.00	−0.0248	0.0918
10	60427.7799	n/a*	7050.00	n/a*	0.0742
11	60555.4750	5907.50	7577.50	−0.0999	0.1546
12	60556.4549	5905.00	7577.50	−0.1002	0.1546
13	60764.7910	n/a*	n/a*	n/a*	n/a*
LCO					
0	60423.5962	6408.88	7161.14	−0.0235	0.0912
1	60430.6106	n/a*	7019.40	n/a*	0.0696
2	60437.5689	6696.40	6907.24	0.0204	0.0525
3	60451.5521	6976.72	6718.67	0.0631	0.0238
4	60465.6034	7036.38	6513.59	0.0722	−0.0075
5	60472.5187	7073.92	6481.86	0.0779	−0.0123
6	60479.5025	7123.15	6450.13	0.0854	−0.0172
7	60493.5267	6890.02	6758.46	0.0499	0.0298
8	60500.5151	6653.91	6842.83	0.0139	0.0427

* n/a indicates values that are not available due to line blending with stationary components or insufficient signal-to-noise ratio, preventing reliable peak identification (see text for details).

Vol. 10709, International Society for Optics and Photonics (SPIE), 107091T

Kotani, T., Kawai, N., Matsuoka, M., & Brinkmann, W. 1996, *Publications of the Astronomical Society of Japan*, 48, 619

Kotani, T., Kawai, N., Yanagisawa, K., et al. 2005, *Nuovo Cimento C Geophysics Space Physics C*, 28, 755

Kubota, K., Ueda, Y., Kawai, N., et al. 2010, *Publications of the Astronomical Society of Japan*, 62, 323

Kurita, M., Kino, M., Iwamuro, F., et al. 2020, *PASJ*, 72, 48

Lang, D., Hogg, D. W., Mierle, K., Blanton, M., & Roweis, S. 2010, *The Astronomical Journal*, 139, 1782

Lodders, K., Palme, H., & Gail, H. P. 2009, *Landolt Börnstein*, 4B, 712

Lopez, L. A., Marshall, H. L., Canizares, C. R., Schulz, N. S., & Kane, J. F. 2006, *ApJ*, 650, 338

Margon, B. 1984, *ARA&A*, 22, 507

Marshall, H. L., Canizares, C. R., Hillwig, T., et al. 2013, *ApJ*, 775, 75

Marshall, H. L., Canizares, C. R., & Schulz, N. S. 2002, *ApJ*, 564, 941

Matsubayashi, K., Ohta, K., Iwamuro, F., et al. 2019, *PASJ*, 71, 102

Medvedev, P. S., Khabibullin, I. I., & Sazonov, S. Y. 2019, *Astronomy Letters*, 45, 299

Medvedev, P. S., Khabibullin, I. I., Sazonov, S. Y., Churazov, E. M., & Tsygankov, S. S. 2018, *Astronomy Letters*, 44, 390

Middleton, M. J., Walton, D. J., Alston, W., et al. 2021, *MNRAS*, 506, 1045

Miller-Jones, J. C. A., Migliari, S., Fender, R. P., et al. 2008, *ApJ*, 682, 1141

Mori, K., Tomida, H., Nakajima, H., et al. 2022, in *Society of Photo-Optical Instrumentation Engineers (SPIE) Conference Series*, Vol. 12181, *Space Telescopes and Instrumentation 2022: Ultraviolet to Gamma Ray*, ed. J.-W. A. den Herder, S. Nikzad, & K. Nakazawa, 121811T

Nagayama, T., & Nakaya, H. 2024, in *Society of Photo-Optical Instrumentation Engineers (SPIE) Conference Series*, Vol. 13096,

- Ground-based and Airborne Instrumentation for Astronomy X, ed. J. J. Bryant, K. Motohara, & J. R. D. Vernet, 130963I
- Nishino, Y., Kimura, M., Sako, S., et al. 2022, PASJ, 74, L17
- Niwano, M., Murata, K. L., Adachi, R., et al. 2021, PASJ, 73, 14
- Noda, H., Mori, K., Tomida, H., et al. 2025, PASJ, arXiv:2502.08030
- Revnivtsev, M., Burenin, R., Fabrika, S., et al. 2004, A&A, 424, L5
- Sakai, Y., Yamada, S., Sakemi, H., et al. 2025, PASJ, 77, 1113
- Sakemi, H., Machida, M., Yamamoto, H., & Tachihara, K. 2023, PASJ, 75, 338
- Sako, S., Ohsawa, R., Takahashi, H., et al. 2018, in Ground-based and Airborne Instrumentation for Astronomy VII, ed. C. J. Evans, L. Simard, & H. Takami, Vol. 10702, International Society for Optics and Photonics (SPIE), 107020J
- Shidatsu, M., Kobayashi, S., Sakai, Y., et al. 2025, PASJ, psaf110
- Shimokawabe, T., Kawai, N., Mori, Y. A., et al. 2009, in American Institute of Physics Conference Series, Vol. 1133, Gamma-ray Burst: Sixth Huntsville Symposium, ed. C. Meegan, C. Kouveliotou, & N. Gehrels (AIP), 79–81
- Sikora, M., Madejski, G., Moderski, R., & Poutanen, J. 1997, ApJ, 484, 108
- Smith, R. K., Brickhouse, N. S., Liedahl, D. A., & Raymond, J. C. 2001, ApJL, 556, L91
- Takagi, T., Shidatsu, M., Okada, Y., et al. 2025, PASJ, accepted
- Tashiro, M. S. 2022, International Journal of Modern Physics D, 31, 2230001
- Tody, D. 1986, in Society of Photo-Optical Instrumentation Engineers (SPIE) Conference Series, Vol. 627, Instrumentation in astronomy VI, ed. D. L. Crawford, 733
- Tonry, J. L., Stubbs, C. W., Lykke, K. R., et al. 2012, ApJ, 750, 99
- Uchida, H., Mori, K., Tomida, H., et al. 2025, PASJ, arXiv:2503.20180
- Valenti, S., Sand, D., Pastorello, A., et al. 2014, MNRAS, 438, L101
- Verner, D. A., Ferland, G. J., Korista, K. T., & Yakovlev, D. G. 1996, ApJ, 465, 487
- Waisberg, I., Dexter, J., Olivier-Petrucci, P., Dubus, G., & Perraut, K. 2019, A&A, 624, A127
- Yatsu, Y., Kawai, N., Shimokawabe, T., et al. 2007, Physica E Low-Dimensional Systems and Nanostructures, 40, 434
- Yoshida, M. 2005, Journal of Korean Astronomical Society, 38, 117